

Document Version

Final published version

Licence

CC BY-NC

Citation (APA)

Christiaanse, J. C., Vitousek, S., Reniers, A. J. H. M., & Antolínez, J. A. Á. (2026). Vulnerability of Key Sea Turtle Nesting Beaches to Future Erosion and Sea Level Rise. *Earth's Future*, 14(3), Article e2025EF007191. <https://doi.org/10.1029/2025EF007191>

Important note

To cite this publication, please use the final published version (if applicable). Please check the document version above.

Copyright

In case the licence states "Dutch Copyright Act (Article 25fa)", this publication was made available Green Open Access via the TU Delft Institutional Repository pursuant to Dutch Copyright Act (Article 25fa, the Taverne amendment). This provision does not affect copyright ownership. Unless copyright is transferred by contract or statute, it remains with the copyright holder.

Sharing and reuse

Other than for strictly personal use, it is not permitted to download, forward or distribute the text or part of it, without the consent of the author(s) and/or copyright holder(s), unless the work is under an open content license such as Creative Commons.

Takedown policy

Please contact us and provide details if you believe this document breaches copyrights. We will remove access to the work immediately and investigate your claim.

Earth's Future

RESEARCH ARTICLE

10.1029/2025EF007191

Key Points:

- Long-term shoreline evolution and seasonality varied considerably across nine global nesting beaches
- Some nesting beaches are stable or building up, while others are eroding with little room to retreat
- Simple “bathtub” methods misrepresent erosion vulnerability, hence dynamic shoreline change must be considered

Correspondence to:

J. C. Christiaanse,
j.c.christiaanse@tudelft.nl

Citation:

Christiaanse, J. C., Vitousek, S., Reniers, A. J. H. M., & Antolínez, J. A. A. (2026). Vulnerability of key sea turtle nesting beaches to future erosion and sea level rise. *Earth's Future*, 14, e2025EF007191. <https://doi.org/10.1029/2025EF007191>

Received 26 AUG 2025

Accepted 12 FEB 2026

Author Contributions:

Conceptualization: Jakob C. Christiaanse

Data curation: Jakob C. Christiaanse

Formal analysis: Jakob C. Christiaanse

Investigation: Jakob C. Christiaanse, Sean Vitousek

Methodology: Jakob C. Christiaanse, José A. A. Antolínez

Resources: Sean Vitousek, José A. A. Antolínez

Software: Jakob C. Christiaanse, Sean Vitousek

Supervision: Ad J. H. M. Reniers, José A. A. Antolínez

Validation: Jakob C. Christiaanse

Visualization: Jakob C. Christiaanse

Writing – original draft: Jakob C. Christiaanse

Writing – review & editing: Jakob C. Christiaanse, Sean Vitousek, Ad J. H. M. Reniers, José A. A. Antolínez

Writing – review & editing: Jakob C. Christiaanse, Sean Vitousek, Ad J. H. M. Reniers, José A. A. Antolínez

Writing – review & editing: Jakob C. Christiaanse, Sean Vitousek, Ad J. H. M. Reniers, José A. A. Antolínez

Writing – review & editing: Jakob C. Christiaanse, Sean Vitousek, Ad J. H. M. Reniers, José A. A. Antolínez

Writing – review & editing: Jakob C. Christiaanse, Sean Vitousek, Ad J. H. M. Reniers, José A. A. Antolínez

© 2026 The Author(s).

This is an open access article under the terms of the [Creative Commons Attribution-NonCommercial License](https://creativecommons.org/licenses/by-nc/4.0/),

which permits use, distribution and reproduction in any medium, provided the original work is properly cited and is not used for commercial purposes.

Vulnerability of Key Sea Turtle Nesting Beaches to Future Erosion and Sea Level Rise

Jakob C. Christiaanse¹ , Sean Vitousek² , Ad J. H. M. Reniers¹ , and José A. A. Antolínez¹ 

¹Department of Hydraulic Engineering, Delft University of Technology, Delft, The Netherlands, ²USGS Pacific Coastal & Marine Science Center, Santa Cruz, CA, USA

Abstract Threatened sea turtles rely on sandy beaches for nesting, linking their long-term survival to global beach availability. However, beaches worldwide are increasingly threatened by anthropogenic stressors and sea level rise (SLR). Reliable vulnerability assessments require understanding beach dynamics across multiple time scales, informed by long-term coastal change records. While many nesting beaches lie in remote, data-poor environments, recent advances in coastal remote sensing now allow us to monitor coastal change worldwide. Here, we combine satellite-derived shorelines (CoastSat), shoreline modeling (CoSMoS-COAST), and global data sets to investigate shoreline evolution and future vulnerability at nine globally important sea turtle nesting sites. We investigate seasonal and long-term shoreline change, hindcast (1980–2024) and forecast (2025–2100) shoreline positions under various SLR scenarios, and quantify available accommodation space based on backbeach elevation and infrastructure footprints. We find that shoreline evolution and vulnerability vary considerably, with three sites showing historical accretion trends and four sites showing erosion. This demonstrates that the previously widely applied bathtub approach—adding SLR to a static beach profile—is not suitable to assess the vulnerability of sea turtle nesting beaches to erosion. Three eroding beaches emerge as particularly vulnerable due to projected shoreline retreat coupled with limited accommodation space. Despite significant uncertainties arising from long-term shoreline projections, our results provide important insights into seasonal and long-term morphodynamics, identify vulnerable nesting sites, and offer a comprehensive, transferable framework for assessing shoreline evolution and relative erosion vulnerability at other sites. Understanding these dynamics is crucial to inform conservation and management strategies to future-proof these critical nesting habitats.

Plain Language Summary Sea turtles depend on sandy beaches for nesting, which means their survival is closely linked to how these beaches change over time. Today, many beaches are increasingly pressured by human activity and rising sea levels, putting turtle nesting habitats at risk. To better understand which beaches are most vulnerable, we used satellite images, computer models, and global data to study nine of the world's most important nesting sites. We looked at how the shoreline has moved since 1980, how it might change through 2100 under different sea level rise (SLR) scenarios, and how much space may remain for turtles to nest given local terrain and development. Our results show that some beaches are naturally building up while others are eroding, and that vulnerability is not the same everywhere. In particular, three beaches appear especially at risk because they are eroding and have little room for turtles to nest further inland. These findings highlight the importance of moving beyond simple “bathtub” estimates of SLR, and instead considering the complex, long-term behavior of beaches. This approach can help identify priority sites for conservation and guide strategies to protect sea turtle nesting habitats in a changing world.

1. Introduction

Sandy beaches cover approximately one-third of the world's ice-free coastline (Luijendijk et al., 2018) and provide a wide range of ecosystem services. They play a critical role in sediment and water retention, serve as buffers against elevated water levels, and offer recreational opportunities. Moreover, they provide essential habitats for sea turtles and shorebirds (Defeo et al., 2009; Nel et al., 2014). Sea turtles, which are key species in many marine ecosystems (e.g., Christianen et al., 2023; Meylan, 1988), rely on these sandy coasts for nesting (Ackerman, 1997). Consequently, the long-term survival of these threatened reptiles is intrinsically tied to the availability of suitable nesting sites around the world. However, sandy beaches worldwide are increasingly threatened by anthropogenic and climatic stressors, such as sea level rise (SLR; e.g., Leaman et al., 2021; Rosati et al., 2013; Vitousek, Barnard, & Limber, 2017). Therefore, there is significant concern about the resilience and

availability of global sea turtle nesting sites in the face of ongoing and future erosion and rising sea levels (Patrício et al., 2021; Rivas et al., 2023).

Sandy beaches are dynamic environments that constantly change in response to a range of stressors such as winds, waves and tides, episodic storm events, interannual climate oscillations, and long-term climate-induced trends (e.g., Antolínez et al., 2018; Ashton et al., 2001; Castelle et al., 2015; Vitousek, Barnard, & Limber, 2017). Beaches generally erode under stormy conditions and recover during low-energy periods, cycling through different beach states across seasons (Wright & Short, 1984). Embayed beaches often show seasonal rotations, owing to changes in wave climate (Abdulsalam et al., 2025; Harley et al., 2015). Interannual oscillations can drive beach change over multiple years (e.g., El Niño/Southern Oscillation, ENSO; Barnard et al., 2015; Vos, Harley, et al., 2023). Structural changes in sediment supply and transport (e.g., through trapping by coastal infrastructure or river damming) can drive chronic erosion/accretion over years to decades (e.g., Pianca et al., 2015). Finally, while beach survivability in response to accelerated SLR is still hotly debated and may vary greatly across different environments (e.g., Cooper et al., 2020; Voudoukas et al., 2020), it is generally understood that accelerated SLR will cause shoreline retreat (Vitousek, Barnard, & Limber, 2017). This may lead to significant long-term beach loss, especially when a static/hardened backbeach environment prevents landward migration of sand (i.e., coastal squeeze; Pontee, 2013).

Sea turtles have survived and nested in dynamic beach environments for millions of years, though over the past centuries, their populations have declined drastically (McClenachan et al., 2006). Their slow population growth rates mean they are less resilient to short-term population declines (Duarte et al., 2020), making them particularly vulnerable to relatively rapid changes (within years to decades) to their nesting habitat (Mortimer, 1995; Pike & Stiner, 2007; Staines et al., 2025). Long-term erosion—from SLR or other causes—could reduce suitable nesting area on the beach, increase the risk of nest flooding, or even lead to the loss of entire nesting beaches. These threats are gaining significant attention in both sea turtle research and conservation efforts (Christiaanse, Reniers, et al., 2025; Hawkes et al., 2009; Patrício et al., 2021). Nature-based solutions—for instance, through turtle-friendly design of sand nourishments (e.g., Smithers & Dawson, 2023) or by restoring vegetation or reefs to provide coastal protection from flooding and erosion (Barbier et al., 2011)—may offer promising opportunities to preserve current nesting beaches and potentially even enable nesting on new beaches (Christiaanse et al., 2024).

To evaluate the need for intervention and design nature-based solutions, we first need to understand how the beach system behaves across different time scales and how vulnerable it is to (future) flooding and erosion. Numerous studies have tried to quantify the potential loss of nesting area to SLR by using a simple bathtub approach—adding a mean sea level increase onto a fixed digital elevation model of the beach (e.g., Fish et al., 2005; Fuentes et al., 2010; Rivas et al., 2023). Although computationally efficient, this approach does not consider any morphological response of the system and therefore does not provide reliable estimates of beach loss (Wolinsky & Murray, 2009). Understanding the vulnerability of nesting beaches to erosion requires long-term observations (e.g., of the shoreline position, which is commonly used to assess beach change across time scales; Splinter & Coco, 2021; Vitousek, Buscombe, et al., 2023), and information on backbeach topography and human development. Yet, many nesting beaches are located in the tropics and in developing countries (Mazaris et al., 2014), where availability of in situ field data is generally low. Fortunately, the advent of publicly available satellite imagery and coastal remote sensing tools now allows us to extract reasonably accurate shoreline observations (order 20–30 m before 2015 and 10 m since) over the past 30–40 yrs anywhere in the world (Bergsma et al., 2021; Vitousek, Buscombe, et al., 2023; Vos, Harley, et al., 2019).

Here, we combine satellite-derived shorelines, shoreline modeling, and global data sets to analyze the shoreline evolution, characteristics, and future vulnerability of nine globally important sea turtle nesting beaches. We use historical shoreline positions extracted from publicly available satellite imagery using CoastSat (Vos, Harley, et al., 2019) to identify seasonal and long-term shoreline change. We calibrate a shoreline model (CoSMoS-COAST; Vitousek, Vos, et al., 2023; Vitousek et al., 2025) with the extracted shorelines to hindcast daily shoreline positions from 1980 to 2024 and forecast them from 2025 to 2100 under various SLR scenarios. Additionally, we quantify the accommodation space at each site using a global coastal digital terrain model (DeltaDTM; Pronk et al., 2024) and global infrastructure footprints (buildings and roads). The shoreline evolution and backbeach characteristics are combined to assess the vulnerability of each site to future erosion and SLR. Our results (a) contribute to the understanding of seasonal and long-term variability of shoreline dynamics at these critical nesting beaches, (b) indicate which sites may be particularly vulnerable to future SLR, and (c) provide a

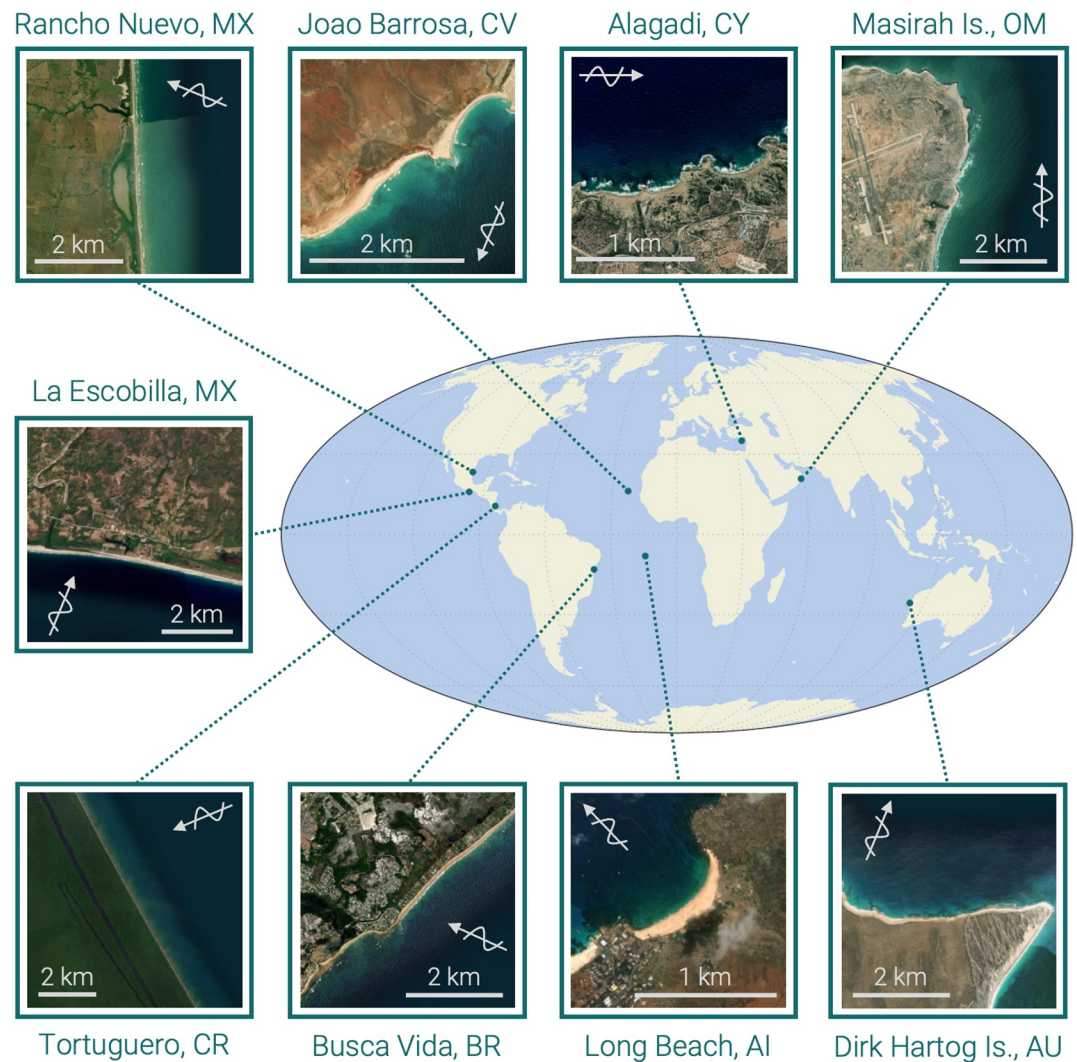


Figure 1. Overview map of the nine nesting sites analyzed in this study. The gray arrow in each panel represents the dominant offshore, deepwater wave direction. Note that waves will therefore not necessarily maintain this direction closer to the shore, but rather refract toward the shoreline. Geographic North is upward in all panels. Satellite snapshots created from Esri World Imagery (Esri, 2024).

comprehensive, transferable framework to analyze shoreline evolution and erosion vulnerability at nesting sites around the world.

2. Methods

2.1. Study Sites

We investigated shoreline evolution and accommodation space at nine key sea turtle nesting sites around the world (Figure 1, Table 1): Long Beach (Ascension Island), La Escobilla (Mexico), Dirk Hartog Island (Australia), Busca Vida (Brazil), Tortuguero (Costa Rica), Alagadi (Cyprus), João Barrosa (Cape Verde), Rancho Nuevo (Mexico), and Maşīrah Island (Oman). We selected these sites because they (a) host large nesting populations and are therefore important nesting sites for their respective species; (b) are relatively remote and lack significant in situ beach evolution data; and (c) exhibit sandy, open-coast morphologies whose long-term evolution is largely unstudied. Together, these criteria allowed us to assess representative nesting-beach types while demonstrating the potential of satellite-derived shoreline analysis to evaluate SLR vulnerability at data-poor and understudied sites.

Table 1
Overview of the Nine Sea Turtle Nesting Sites Analyzed in This Study

Site	Country	Lon/Lat	Beach type	Main species	Nest season	\bar{H}_s	Tide
Long Beach	Ascension Is.	−14.41, −7.92	Embayed	<i>Cm</i>	1–6	1.8	0.9
La Escobilla	Mexico	−96.73, 15.72	Open	<i>Lo</i>	8–11	1.4	1.2
Dirk Hartog Is.	Australia	112.99, −25.5	Embayed	<i>Cc</i>	11–4	2	0.9
Busca Vida	Brazil	−38.27, −12.87	Open	<i>Ei</i>	10–3	1.1	1.7
João Barrosa	Cabo Verde	−22.71, 16.03	Open/embayed	<i>Cc</i>	6–11	1.4	0.7
Tortuguero	Costa Rica	−83.47, 10.48	Open (BI)	<i>Cm</i>	7–10	0.9	0.3
Alagadi	Cyprus	33.49, 35.34	Embayed	<i>Cm, Cc</i>	5–10	0.8	0.3
Rancho Nuevo	Mexico	−97.77, 23.18	Open (BI)	<i>Lk</i>	4–7	0.9	0.5
Maşrah Is.	Oman	58.91, 20.66	Open/embayed	<i>Cc</i>	5–9	1	2

Note. The abbreviation BI in the beach type stands for Barrier Island. Nesting season is specified in month numbers. The last two columns show the mean significant wave height (\bar{H}_s) and the mean tidal range, both in meters. Species abbreviations are: *Cm*, *Chelonia mydas*; *Cc*, *Caretta caretta*; *Ei*, *Eretmochelys imbricata*; *Lk*, *Lepidochelys kempii*, and *Lo*, *Lepidochelys olivacea*.

We describe the results of the first two sites (Long Beach and La Escobilla) in detail in the main text of this paper, while the other seven locations are briefly discussed and summarized. Detailed site descriptions and results figures for the seven remaining sites are provided in Appendix A and Appendix D, respectively.

2.1.1. Long Beach, Ascension Island

Ascension Island is an isolated volcanic peak on the mid-Atlantic ridge, which hosts one of the largest green sea turtle (*Chelonia mydas*, *Cm*) nesting populations in the world (Weber et al., 2014). Long Beach, a 1 km-long embayed beach on the island's north–west side, is the largest beach and supports the highest number of nests (Godley et al., 2001). The main nesting season spans from January to June. The tidal range is relatively small (0.9 m), but the island is exposed to high wave energy (mean $H_s \approx 1.8$ m), with mostly persistent south-easterly swells from trade winds and less frequent but larger westerly swells. Being situated on the north–west side of the island, Long Beach is partly sheltered from the dominant south-easterly swells.

2.1.2. La Escobilla, Mexico

La Escobilla covers a 7-km long stretch of open sandy beach on the southern Pacific coast of Mexico. It is one of only several olive ridley (*Lepidochelys olivacea*, *Lo*) mass-nesting (*arribada*) beaches worldwide and therefore is an extremely important nesting site for the species (Ocana et al., 2012). In fact, La Escobilla hosts the largest sea turtle nesting aggregation in the world, with up to 1 million olive ridleys nesting in just a few days (Mast et al., 2025). The main nesting season ranges from August to November. Several small rivers and lagoons span the length of the beach. The tidal range (1.2 m) and wave climate (mean $H_s \approx 1.4$ m) are moderate, though the beach is fully exposed to the dominant long-period southwesterly swells.

2.2. Data and Indicators

2.2.1. Coastal Transects (GCTS)

We used the Global Coastal Transect System (GCTS; Calkoen et al., 2025) to extract roughly shore-normal transects every 100 m along each nesting beach. For nesting beaches longer than 5 km, we limited the analysis to a roughly 5-km long stretch. When spatial nesting data were available from literature we tried to select the stretch with the highest nesting density, otherwise we investigated a stretch around the center of the beach. We then selected three representative transects from the available GCTS transects, generally near the middle and the two ends of the (5-km-stretch of) beach. The analyses were carried out by intersecting the transects with the satellite-derived shorelines, elevation data, and infrastructure footprints to define relevant positions along the transects (see following sections).

2.2.2. Satellite-Derived Shorelines (CoastSat)

We used the Python-based toolbox CoastSat to extract shorelines from publicly available satellite imagery, described in detail in Vos, Splinter, et al. (2019). Briefly, CoastSat downloads satellite images (Landsat 5, 7, 8, 9, and Sentinel 2) through Google Earth Engine (Gorelick et al., 2017) for a user-defined region of interest and pre-processes them (e.g., by removing cloudy pixels and applying pan-sharpening for enhanced resolution). Each pixel is then classified into “water”, “white-water”, “sand”, or “other”, using a Neural Network classifier. This classification is used in combination with the Modified Normalized Difference Water Index (MNDWI; Xu, 2006) to extract a sub-pixel resolution shoreline contour, that best separates the “sand” and “water” classes (Vos, Harley, et al., 2019). The shorelines are then mapped to user-defined transects. Given that the individual satellite images capture the beach at varying tidal levels, the shoreline positions are tide-corrected using tidal data from the global FES2022 tide model (CNES, 2024). The CoastSat.Slope module can be used to estimate the beach-face slope by tide-correcting the shoreline time series for a range of potential slope values, and selecting the one that results in the highest damping of the tidal frequencies in the shoreline signal (Vos et al., 2020).

We used all available images from 1984 to the end of 2024 (41 yrs) from all available satellite missions (Landsat 5, 7, 8, 9, and Sentinel 2). We used the default parameters along with several manual settings per study site (e.g., cloud cover threshold, maximum deviation from reference shoreline), which are detailed in Appendix B along with the total number of images acquired for each site. We could not validate the extracted shoreline positions due to a lack of in situ beach survey data, but we carried out visual inspections of the mapped shorelines on the corresponding satellite images. Moreover, CoastSat-derived shorelines have been validated and compared to in situ observations in several studies, across different environments and beach settings, generally resulting in a shoreline position error in the order of 10–15 m (Castelle et al., 2021; Vos, Harley, et al., 2019, 2023; Vos, Splinter, et al., 2023). They are less accurate on macro-tidal, high-energy beaches (Castelle et al., 2021), but all our study sites were micro-tidal, except Maşīrah Island (meso-tidal, Table 1). Finally, CoastSat-derived shorelines have been successfully used to study beach behavior from seasonal to decadal time scales at many locations (e.g., Castelle et al., 2022; Vos, Harley, et al., 2023; Warrick et al., 2025).

We mapped the extracted shorelines to the GCTS transects to obtain time series of the relative shoreline position at each transect. Outliers were filtered using CoastSat's built-in `SDS_transects.reject_outliers()` function. We estimated the beach slope using CoastSat.Slope during the tidal correction. The shorelines were not corrected for any residual water level differences (e.g., storm surge). Finally, we computed a reference shoreline position by taking the median (less sensitive to extremes/outliers than the mean) shoreline position between 2021 and 2024 (i.e., representing the current shoreline position).

2.2.3. Accommodation Space

To quantify the current accommodation space available at each study site, we used three distance indicators, all relative to the reference shoreline position: the backbeach distance (BBD), the infrastructure-free distance (IFD), and the beach width (Figure 2). An elevation profile of the backbeach along each transect was extracted from DeltaDTM—a state-of-the-art digital terrain model that covers the global coastal regions between 0 and 30-m elevations (Pronk et al., 2024). DeltaDTM has a horizontal resolution of 1 arcsecond (≈ 30 m) and a vertical mean absolute error of 0.45 m. We computed the distance between the first point along each transect above 10 m + MSL elevation and the reference shoreline position as BBD.

To compute the IFD, we used building and road footprints from Overture maps (www.overturemaps.org). Road footprints from Overture mainly come from OpenStreetMap (www.openstreetmap.org/copyright) and are divided into hierarchical categories, from highways to walking paths. Due to the high number of classes, we summarized them into highway (highways and trunks), major road (primary and secondary roads), minor road (tertiary and residential roads), and cycle/walking paths (all remaining roads). As IFD, we computed the distance along each transect from the reference shoreline position to the first intersection with a highway, major road, or building (i.e., the shortest distance was used as IFD, similar to Lansu et al., 2024). We excluded the minor road and foot/cycle categories as they do not necessarily represent fixed obstacles to future shoreline migration. Because the scattered building footprints often fall in-between transects, we used a 50-m buffer zone around each transect to determine intersecting buildings.

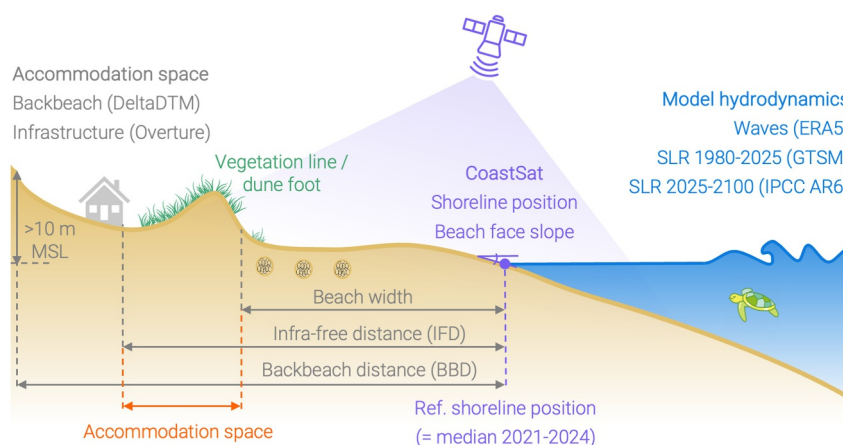


Figure 2. Schematic cross-shore profile of a nesting beach (not to scale), showing the various indicators and data sets used in this study. The accommodation space is computed by subtracting the beach width from the lesser of the infrastructure-free distance (IFD) and the backbeach distance (BBD).

The shortest distance of the BBD and IFD represented the maximum available space for shoreline retreat. However, if the shoreline were to retreat this entire distance, there would be no beach remaining. Therefore, we estimated the current beach width by intersecting each transect with a manually digitized vegetation edge/dune foot line. To draw this line, we used the most recent Google Earth image at each site and followed the first clear vegetation line behind the beach. For João Barrosa and Maşirah Island there was no clear vegetation line, so we estimated the dune foot from high-resolution satellite imagery, Google Street View, and public images of the beach, if available. As final proxy of the available accommodation space, we subtracted the beach width from the shortest distance, IFD or BBD (Figure 2). Hence, this approach assumes that the beach would only start narrowing once the accommodation space is exceeded.

2.3. Shoreline Model (CoSMoS-COAST)

The shoreline-change model used here is a recent update of CoSMoS-COAST (Vitousek, Barnard, Limber, Erikson, & Cole, 2017; Vitousek et al., 2021; Vitousek, Vos, et al., 2023), a transect-based, data-assimilated model, which integrates long- and cross-shore sediment transport processes. We calibrated CoSMoS-COAST with historical wave conditions and satellite-derived shoreline positions over a hindcast period from 1980 to 2024. Next, we ran forecast simulations (2025–2100) to project long-term shoreline change and assess erosion vulnerability at the three selected transects within each study site.

While there are many shoreline models available, we chose CoSMoS-COAST because its data assimilation method works particularly well with satellite-derived shoreline data and it performed consistently well in a recent benchmarking study (Mao et al., 2025). Moreover, we decided to focus the modeling on the shoreline only instead of including dune dynamics, which would have been possible with a model like COCOONED (Antolínez et al., 2019). For a more detailed description and objective comparison of many current shoreline models (including CoSMoS-COAST and COCOONED) we refer to Mao et al. (2025) and Montañó et al. (2020).

2.3.1. Model Equation, Parameters, and Calibration

The governing equation of CoSMoS-COAST is based on the one-dimensional conservation of sediment volume equation:

$$\frac{\partial Y}{\partial t} = \frac{Y_{eq} - Y}{\tau} - \frac{1}{d_c} \frac{\partial Q}{\partial X} - \frac{c}{\tan \beta} \frac{\partial S}{\partial t} + v_{lt}, \quad (1)$$

where the left-hand term is the rate of change in the shoreline position Y with respect to time t , and the four terms on the right-hand side represent: (a) wave-driven cross-shore equilibrium shoreline change (after Yates et al., 2009; Vitousek et al., 2021), where Y_{eq} is the equilibrium shoreline position (set by instantaneous wave

Table 2
Overview of the Seven Model Parameters That Need to be Calibrated in the CoSMoS-COAST Shoreline Model

Parameter	Symbol	Unit	Lower bound	Upper bound
Cross-shore equilibrium timescale	ΔT_{cs}	days	20	300
Cross-shore equilibrium excursion	ΔY_{cs}	m	2	100
Longshore equilibrium timescale	ΔT_{ls}	days	20	365
Longshore equilibrium excursion	ΔY_{ls}	m	-250	250
Bruun coefficient	c	-	0.5	1.5
Residual linear trend	v_{lt}	m/y	-1	1
Initial shoreline position	Y_0	m	-70	70

Note. The final two columns denote the bounds of the calibration range.

conditions) and τ the equilibrium timescale; (b) gradients in longshore transport, where d_c is the depth of closure, Q is the longshore transport, and X is the alongshore coordinate; (c) sea-level driven profile recession (i.e., the Bruun rule), where S is the sea level, $\tan \beta$ is the transgression slope, and c a recession coefficient; and (d) a linear residual trend. See Vitousek, Barnard, Limber, Erikson, and Cole (2017); Vitousek et al. (2021); Vitousek, Vos, et al. (2023) for details on each model component and its parameters.

Although the underlying Equation 1 and unknown model parameters (Table 2) of the CoSMoS-COAST model used here (and also in Mao et al., 2025) are the same as in Vitousek, Vos, et al. (2023), the numerical-solution technique and parameter-estimation method differ from the original. The current model reformulates the cross-shore and longshore-transport terms as discrete convolution operations (see Vitousek et al., 2025; Mao et al., 2025, for details), resulting in the following equation for the shoreline position Y at time t :

$$Y(t) = Y_0 + f_{cs}(t) * g_{cs}(t) + f_{ls}(t) * g_{ls}(t) - c \frac{S(t) - S_0}{\tan \beta} + v_{lt}t, \quad (2)$$

where Y_0 is the initial shoreline position, $*$ represents a convolution operation, $f_{cs}(t)$, $g_{cs}(t)$ and $f_{ls}(t)$ and $g_{ls}(t)$ are the cross-shore and longshore convolution functions, respectively, given by:

$$f_{cs}(t) = -\Delta Y_{cs} \frac{H_s^2(t) - \bar{H}_s^2}{\bar{H}_s^2}, \quad (3)$$

$$g_{cs}(t) = \left(1 - \frac{\Delta t}{\Delta T_{cs}}\right)^{t/\Delta t}, \quad (4)$$

$$f_{ls}(t) = \Delta Y_{ls} \sin(2\alpha(t)), \quad (5)$$

$$g_{ls}(t) = \left(1 - \frac{\Delta t}{\Delta T_{ls}}\right)^{t/\Delta t}, \quad (6)$$

where H_s is the significant wave height, Δt the model time step (1 day), and α the wave incidence angle relative to the shoreline angle.

The seven unknown model parameters resulting from Equations 2–6 are summarized in Table 2. The current model is calibrated using a constrained optimization routine (see upper and lower parameter bounds in Table 2), not the ensemble Kalman filter method of the original model (Vitousek, Vos, et al., 2023). The new (iterative) optimization method was tailored to simulate a smaller number of independent transects, whereas the original (sequential, non-iterative) method was designed to run over $\mathcal{O}(1,000\text{--}10,000\text{s})$ of transects, for which an iterative optimization method would have been too costly. The parameter-estimation routine used here minimizes the loss function:

$$\mathcal{L}_i = \sqrt{RMSE_{\text{norm}}^2 + (1 - \rho)^2 + (1 - STD_{\text{norm}})^2} \quad (7)$$

for each transect i , individually, where

$$RMSE_{\text{norm}} = \frac{RMSE_{\text{mod}}}{STD_{\text{obs}}} = \frac{\sqrt{\frac{1}{N} \sum_{n=1}^N (Y_{\text{obs}_n} - Y_{\text{mod}_n})^2}}{STD_{\text{obs}}}, \quad (8)$$

$$STD_{\text{norm}} = \frac{STD_{\text{mod}}}{STD_{\text{obs}}}, \quad (9)$$

and ρ are the normalized root mean square error, the normalized standard deviation, and the Pearson correlation coefficient, respectively. The subscripts $_{\text{obs}}$ and $_{\text{mod}}$ denote observed and modeled values.

2.3.2. Forcing and Model Scenarios

We first calibrated the model over the entire hindcast period (1980–2024). To force the model, we used historical time series of parametric offshore wave conditions from the global ERA5 reanalysis (Hersbach et al., 2018) and SLR from the Global Tide and Surge Model v3.0 (GTSM; Muis et al., 2020). For waves, we extracted the daily maximum significant wave height (H_s) and corresponding mean wave direction (θ) from the nearest ERA5 node at each study site. Offshore wave conditions were used because reliable bathymetry data required to compute nearshore wave propagation are not available at the study sites; this is accounted for during model calibration. For historical SLR, we extracted the yearly mean sea level at the nearest GTSM node. Thus, the wave conditions were updated at each timestep (daily), whereas the mean sea level was updated each year.

Given the inherent noise and error in satellite-derived shorelines (Vitousek, Buscombe, et al., 2023; Vos, Harley, et al., 2019), we applied a density-based filter and smoothed the obtained shorelines before feeding them into the model: first, we removed all years with less than five observations to decrease the chance of isolated observations disproportionately affecting the long-term trend. These were mainly years in the early part of the period (before the launch of Landsat 7 in 2000). Next, we smoothed the shorelines using the `smoothn` Matlab function (smoothing parameter $S = 30$; Garcia, 2010). Then, the optimization routine searched for the set of model parameters that minimize the multivariate loss function (Equation 7) using the modeled shorelines and the smoothed shoreline time series in the hindcast period.

For the forecast period (2025–2100), we used the model with the optimized parameter values obtained during the hindcast period. We extracted decadal SLR rates from the nearest node of the regional IPCC AR6 SLR projections (Fox-Kemper et al., 2023). To account for scenario and SLR modeling uncertainty we ran the model for the 5th, 50th, and 95th percentile of a low emission scenario (SSP1–2.6) and a very high emission scenario (SSP5–8.5) of the low confidence AR6 projections (which include both low and medium confidence processes; Garner et al., 2021; Kopp et al., 2023). The 50th percentile represented the median projections, while the 5th and 95th percentiles were used to determine a 90% confidence interval. We interpolated decadal to yearly rates and cumulatively added these to the mean sea level between 2021 and 2024 derived from GTSM (i.e., the final 4 yrs of the hindcast period).

To keep the scope focused on SLR impacts, we did not explicitly account for projected future changes in wave climate, which come with significant additional uncertainty (e.g., Morim et al., 2019; Reguero et al., 2019). Instead, to create the future wave time series, we drew a random month from the 45-year ERA5 time series (1980–2024) for each month starting from January 2025 (i.e., for January 2025, we drew a random January between 1980 and 2024, then a random February, and so on, following the method of Davidson et al., 2010). Hence, the future wave time series were shuffled versions of the ERA5 time series.

All forecast simulations use the fully calibrated CoSMoS-COAST model, thereby retaining the seasonal and interannual shoreline variability learned during the hindcast, even though only the long-term components are emphasized in some figures for clarity.

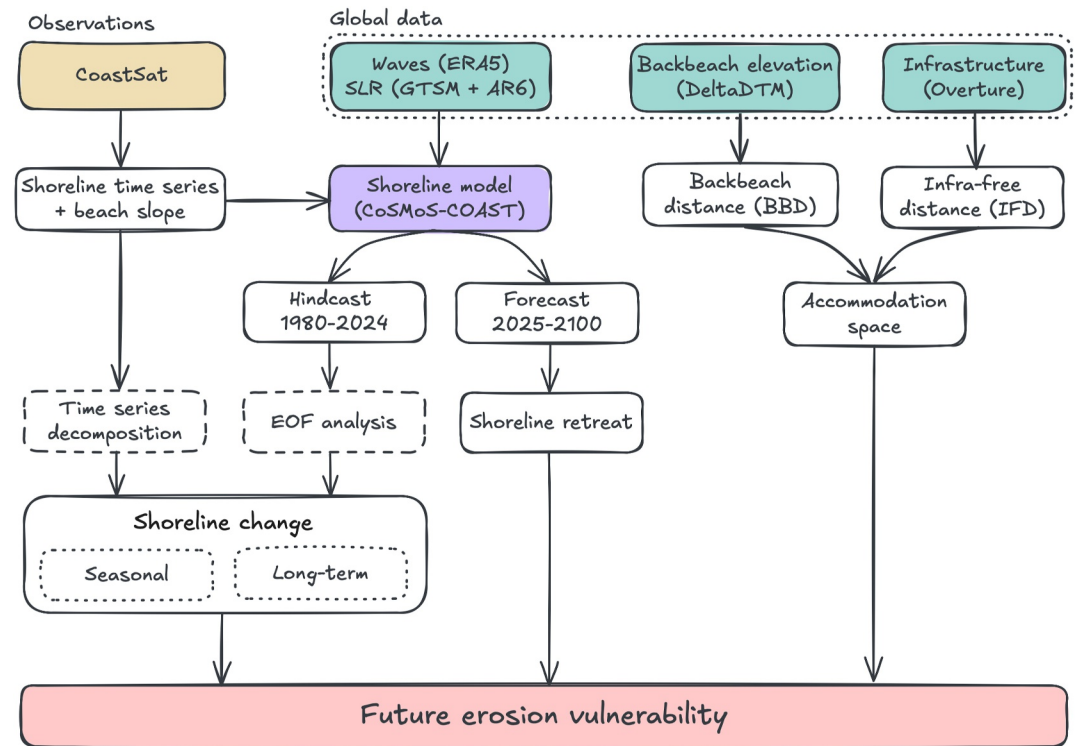


Figure 3. Flowchart showing the approach used in this study. The future erosion vulnerability of the nine nesting beaches is assessed by combining historical shoreline change (satellite-derived and hindcasted), modeled shoreline projections, and an estimate of the accommodation space.

2.3.3. Performance Verification

Model calibration was performed over the full hindcast period using the CoastSat-derived shoreline timeseries. Because no independent in situ shoreline observations were available at the study sites, a separate blind validation data set could not be defined. Therefore, we evaluated the model performance with the same shoreline time series used for calibration. In this context, the model is intended to capture dominant seasonal to long-term shoreline behavior and support relative vulnerability assessments rather than provide precise deterministic predictions of future shoreline position.

As model performance is known to depend on the chosen metric (Montaño et al., 2020), we used two widely applied methods (e.g., Gomez-de la Peña et al., 2023; Montaño et al., 2020; Repina et al., 2025): (a) Mielke's index, λ , which ranges between 0 (poor) and 1 (perfect performance); and (b) Taylor diagrams (Taylor, 2001), which allow a graphical comparison of modeled and observed shoreline behavior based on their normalized standard deviation (STD_{norm}), Pearson's correlation (ρ), and normalized root mean squared error ($RMSE_{norm}$)—i.e., the same metrics as used in the optimized loss function (Equation 7). Mielke's index was computed as (Duveiller et al., 2016):

$$\lambda = 1 - \frac{\frac{1}{N} \sum_{n=1}^N (Y_{obs_n} - Y_{mod_n})^2}{STD_{obs}^2 + STD_{mod}^2 + (\bar{Y}_{obs} - \bar{Y}_{mod})^2}, \quad (10)$$

where N is the number of observed (Y_{obs}) and modeled (Y_{mod}) shoreline positions, \bar{Y}_{obs} and \bar{Y}_{mod} are the mean values, and STD_{obs} and STD_{mod} the standard deviations. The numerator represents the mean squared error (MSE).

2.4. Shoreline Evolution Analysis

To assess the shoreline evolution and erosion vulnerability of the nine sites, we used the CoastSat-derived shoreline positions and the model hind- and forecasts. First, we decomposed the CoastSat-derived time series to derive

seasonal and long-term components. Then, we used Empirical Orthogonal Function (EOF) analysis on the model hindcast. The full approach is visualized in Figure 3 and explained in more detail in the following paragraphs.

2.4.1. Shoreline Time Series Decomposition

To analyze seasonal to long-term trends in the satellite-derived shoreline positions, we used Seasonal-Trend Decomposition based on LOESS (STL; Cleveland et al., 1990), where LOESS stands for Locally Estimated Scatterplot Smoothing (W. S. Cleveland, 1979). Using STL, the CoastSat-derived shoreline position time series at each transect was decomposed into three components:

$$Y(t) = Y_{lt}(t) + Y_{ss}(t) + Y_{res}(t), \quad (11)$$

where Y_{lt} is the long-term trend, Y_{ss} is the recurring seasonal component, and Y_{res} is the residual shoreline position.

First, we derived Y_{lt} using LOESS (Python library *loess* by Cappellari et al., 2013) with a 4-year smoothing window, in order to separate interannual to decadal variability in shoreline change from seasonal fluctuations (as in Warrick et al., 2025). LOESS requires regular sampling intervals without gaps, for which we used the median monthly shoreline position. We linearly interpolated gaps of up to nine consecutive months. If there were larger gaps, we only used the most recent part of the time series, with gaps of 9 months or less. Interpolated values were only used in the derivation of Y_{lt} , not the seasonal component. We then detrended the time series by removing Y_{lt} , leaving the seasonal and residual components. The seasonal component (Y_{ss}) was then computed from the bulk monthly median shoreline position over the remaining time series (i.e., the median position per month over all years). We estimated the seasonal shoreline excursion as the difference between the maximum and minimum position in the seasonal cycle. Finally, subtracting Y_{ss} from the detrended time series yielded the residual component ($Y_{res} = Y - Y_{lt} - Y_{ss}$). Interannual variability in the seasonal cycle is therefore included in Y_{res} .

While Y_{lt} provided some means of visually assessing long-term shoreline change, it still included some of the interannual signals. Therefore, we also quantified the total long-term shoreline change rate at each site through (a) a linear regression fit to the smoothed CoastSat observations (i.e., the same data as used for the model hindcast) and (b) the long-term trend (v_{lt}) from the model, which was capped at 1 m of shoreline change per year (Table 2).

2.4.2. EOF Analysis on Shoreline Hindcast

We performed EOF analysis on the modeled daily shoreline positions to further assess the dominant modes of shoreline change over the hindcast period (45 yrs, 1980–2024). For a complete technical description of EOF applied to shoreline analysis, see Miller and Dean (2007b). Briefly, the eigenvector decomposition was applied on the covariance matrix of spatio-temporal shoreline positions. Hence, EOFs describe the main spatial shoreline change modes, including their temporal amplitudes (given by the principal components, PCs). This allows quantifying how the shoreline positions at different transects change over time (Antolínez et al., 2019; Miller & Dean, 2007a, 2007b). The number of EOFs/PCs is equal to the smallest dimension (in this case three EOFs across the three transects per study site).

3. Results

3.1. Long Beach, Ascension Island

Due to the remoteness of Ascension Island, there were no images from Landsat 5 and only very few from Landsat 7. From 2013/14 (post-Landsat 8 launch), image frequency increased, leaving 12 yrs of data for the shoreline decomposition ($n = 400$ shorelines after outlier removal, Figures 4f–4h). As can be seen from the seasonal cycles at the three transects, Long Beach is a perfect example of a rotating pocket beach: transect T3 erodes during the austral winter (higher wave energy), while the more sheltered T1 accretes during the same period (Figures 4b and 4e–4h). At both transects, the total seasonal shoreline excursion was around 45 m. At T2, the seasonal excursion was less (19 m), being closer to the pivot point of the beach rotation. The nesting season mostly overlapped with the widest beach at T3 (austral summer) but extended well into the rotation of the beach. Over the past 12 yrs, the long-term trend appeared relatively stable, with some interannual variability and a weak erosive trend at T2 and T3.

The backbeach elevation and accommodation space varied significantly in alongshore direction (i.e., across the transects; Figures 4c and 4d). At the northern end (T1) the backbeach was flatter and only started steepening about

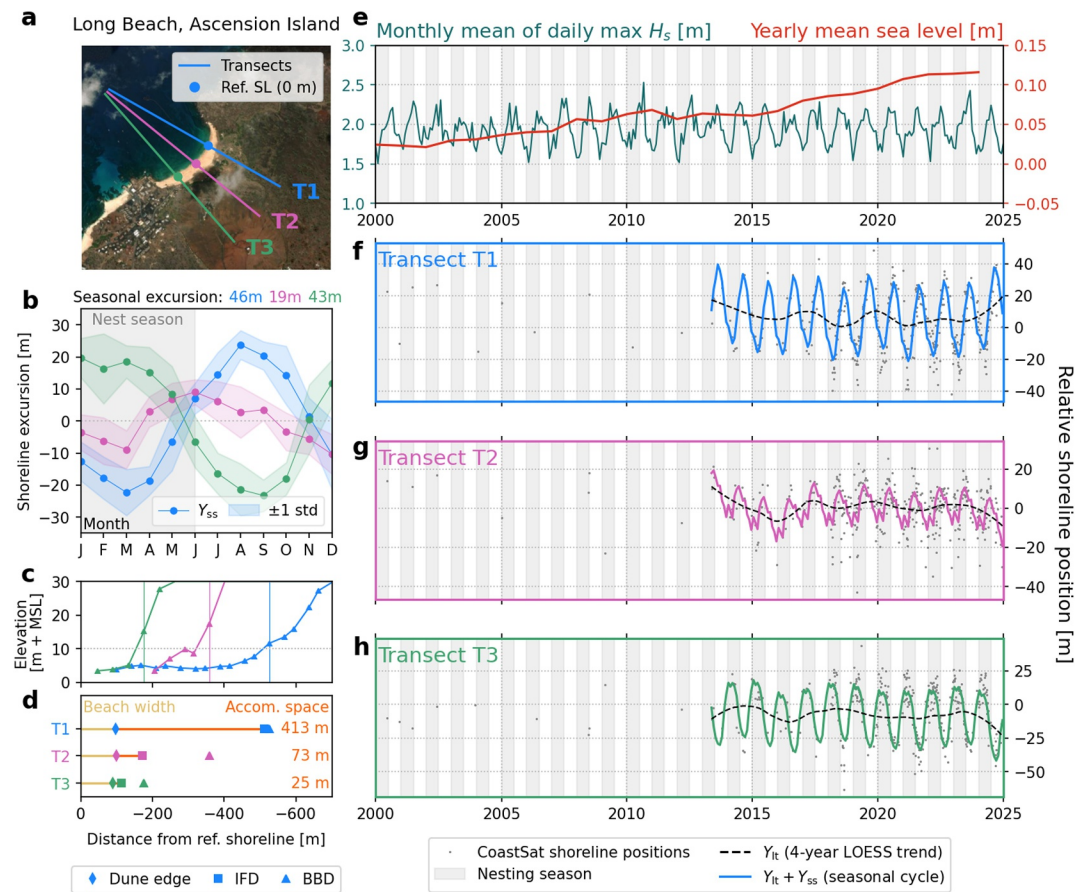


Figure 4. Shoreline and accommodation space analysis for Long Beach, Ascension Island: (a) Satellite image showing the transects and reference shoreline position (Ref. SL); (b) Seasonal shoreline component, Y_{ss} , at each transect; (c) Backbeach elevation profiles, with vertical lines denoting the first point above 10 m + MSL; (d) Beach width and accommodation space at each transect; (e) Historical wave and water level time series; (f, g) Observed and decomposed (long-term and seasonal) shoreline position time series at each transect. Satellite snapshot created from Esri World Imagery (Esri, 2024).

400–500 m from the reference shoreline. Moving south, the backbeach profile became increasingly steep with a sharp increase in the slope around 150 m from the shoreline at T3, owing to a hill behind the southern part of the beach. The median beach width was about 100 m at T1 and T2 and 90 m at T3. Though the backbeach is not highly developed, the accommodation space at all three transects was determined by buildings behind the beach, with the least space at T3 (25 m) and T2 (73 m) and significantly more space at T1 (413 m, Figure 4d). Considering the backbeach elevation only, the accommodation space would have increased to about 350 and 80 m at T2 and T3, respectively.

The model performed differently across the three transects but generally matched the observed seasonal cycles (Figure 5b). Especially at T3, the model aligned well with the observations and had a relatively low root-mean-square-error ($RMSE = 10$ m) compared to the fluctuations in the signal ($\mathcal{O}(50$ m)). At T1 and T2, the model still achieved reasonable RMSE values but struggled to fully capture the seasonal and interannual variability, especially at T1. At T2, the RMSE was smaller than at T3, but the signal fluctuations were also substantially smaller (i.e., the relative RMSE was larger at T2). Over the past 45 yrs, the hindcast showed long-term erosion at all transects, though strongest at T2 (≈ 0.5 m/year). This suggests the beach was less curved in the past, with the shoreline at T2 further seaward relative to T1 and T3.

The EOF analysis confirmed the beach rotation as the dominant mode of change, represented by EOF 1 (68% of the variance). It clearly showed the seasonal oscillation in the PC amplitude over time and the corresponding opposite EOF coefficients at T1 and T3 (Figures 5c and 5d). EOF 2 ($\approx 29\%$) represented a combination of a seasonal to interannual cross-shore mode in which all transects erode/accrete simultaneously, and the long-term erosive trend,

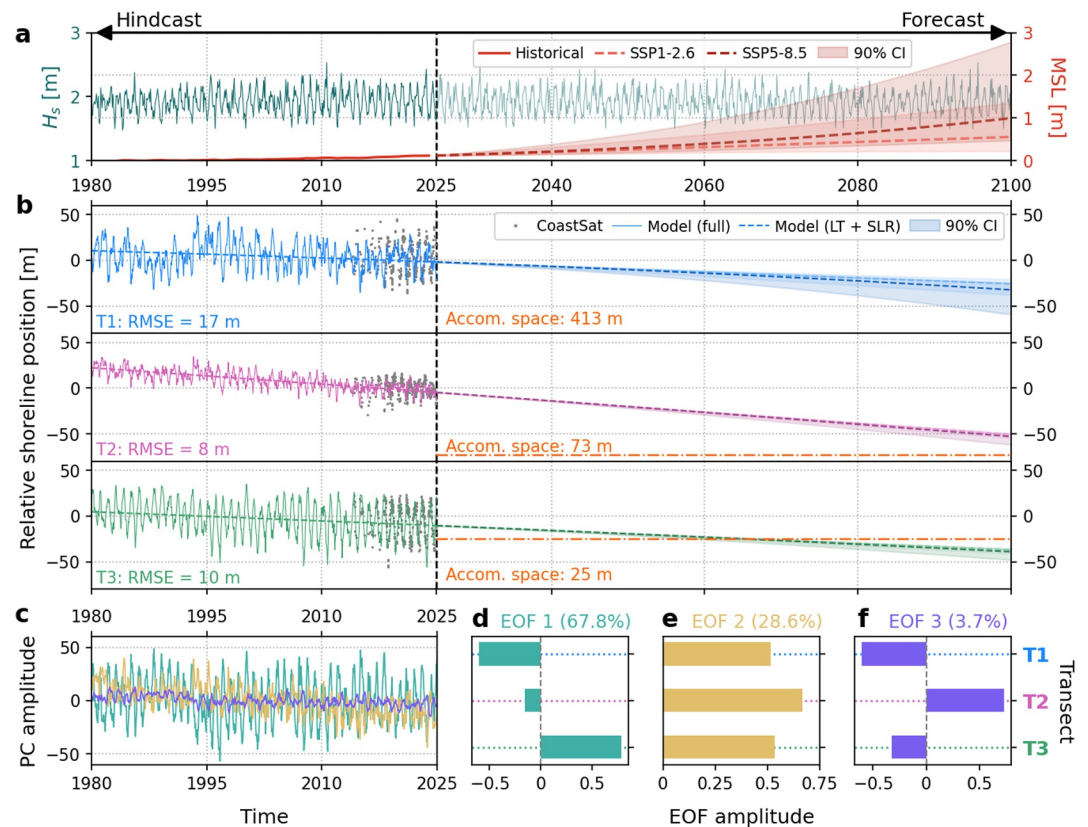


Figure 5. Shoreline modeling results at Long Beach, Ascension Island. (a) Wave and sea level time series used to force the model; (b) Modeled shoreline position at each transect for the hindcast (1980–2024) and forecast (2025–2100) periods. Gray dots are the CoastSat shorelines, solid lines represent the full model results, and dashed lines only include the long-term trend (v_{lt}) and sea level rise (SLR) components. In the forecasts, the two dashed lines represent the median SSP1–2.6 (lighter color) and SSP5–8.5 (darker color) SLR projections, while the shading indicates the area between the 5th and 95th percentile; (c) Amplitude of the three PCs over the hindcast period; (d–f) Amplitudes of the three EOFs at each transect and percentage of explained variance.

which was strongest at T2 (highest EOF amplitude; Figures 5c and 5e). Although EOF 3 only explained about 4% of the variance, it represented part of the reorientation of the beach (from straighter to more curved), with T2 eroding and T1 and T3 accreting (Figures 5c and 5f; no net accretion as in EOF 2 both T1 and T3 eroded).

The model predicted future erosion at all three transects, but to differing degrees. T2 was the most erosive with at least 50 m of shoreline retreat projected by 2,100, under both median SLR scenarios, significantly reducing the available accommodation space (Figures 5a and 5b). The median projections were slightly less erosive at T1 and T3, though at T1 the 90% confidence intervals covered a larger spread, with the SSP5–8.5 95th percentile also predicting more than 50 m shoreline retreat. At T3 the difference between SLR scenarios was relatively small, with around 35–50 m of shoreline retreat by 2,100. More importantly, shoreline retreat at T3 was projected to exceed the available accommodation space of 25 m around 2060/70.

3.2. La Escobilla, Mexico

At La Escobilla there was sufficient data for the STL shoreline decomposition from 1993 onward (32 yrs and $n = 1016$ shorelines after outlier removal, Figures 6f–6h). Again, there was a clear seasonal pattern in the shoreline position, with the excursion around 25 m at all transects (Figure 6b). Instead of a rotating beach, La Escobilla showed a dominant cross-shore mode, with all transects accreting and eroding in phase with each other. The entire beach narrowed in the austral winters, during the peak of the southern hemisphere swell, and widened in the austral summers. This means the beach is relatively narrow when turtle nesting starts in August, but widens as the nesting season progresses.

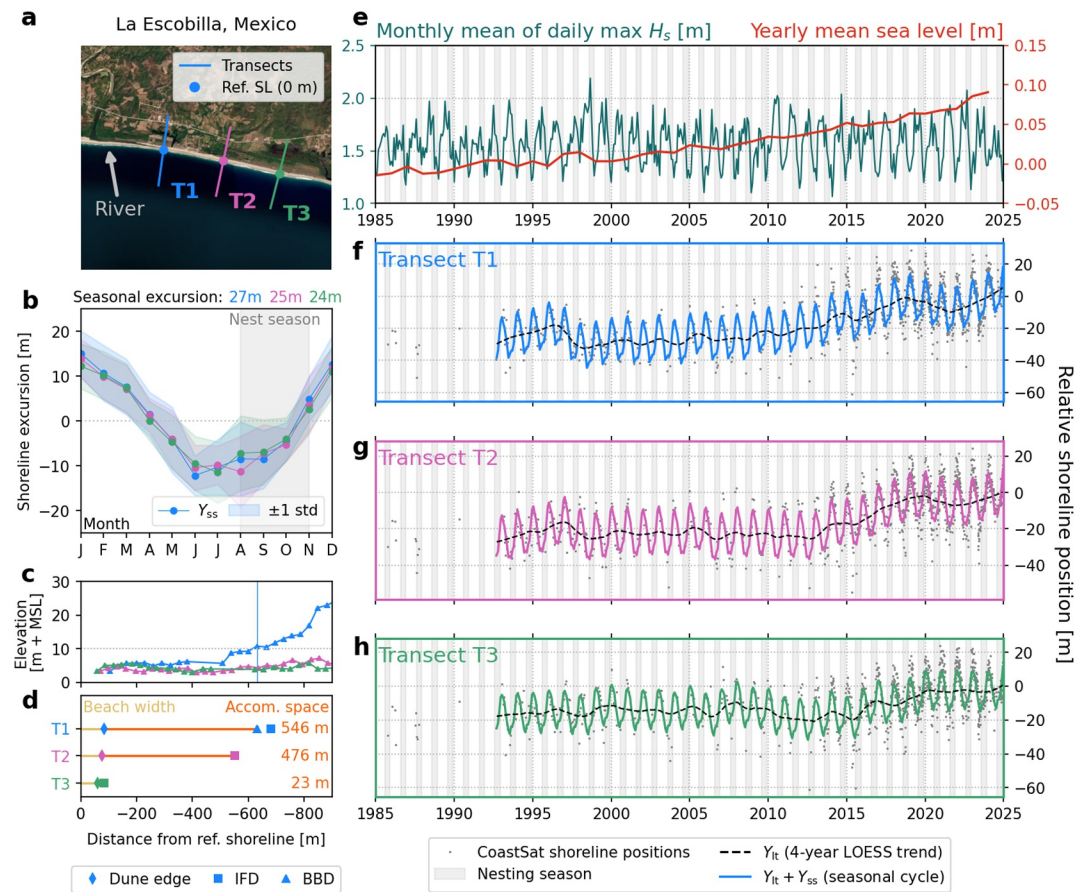


Figure 6. Shoreline and accommodation space analysis for La Escobilla, Mexico: (a) Satellite image showing the transects and reference shoreline position (Ref. SL); (b) Seasonal shoreline component, Y_{ss} , at each transect; (c) Backbeach elevation profiles, with vertical lines denoting the first point above 10 m + MSL; (d) Beach width and accommodation space at each transect; (e) Historical wave and water level time series; (f–h) Observed and decomposed (long-term and seasonal) shoreline position time series at each transect. Satellite snapshot created from Esri World Imagery (Esri, 2024).

Although mean sea level at La Escobilla increased by about 10 cm since 1985 (Figure 6e), the shoreline data showed a long-term accretion trend—strongest at T1 since about 2000 (≈ 1 m/year), and at T2 and T3 mostly over the past decade (Figures 6f–6h). Between 1993 to about 2010–15, the long-term shoreline position was relatively stable at T2 and T3, with some interannual oscillations. Since then, the beach has generally accreted. There have been no beach nourishments near this site, but one explanation for the accretion could be that the river to the west of T1 has been supplying the beach with sediment (Figure 6a). This hypothesis was supported by the eastward movement of the river channel on the beach, apparent in historical satellite images. This suggests alongshore sediment transport is eastward, which could also explain the lag in the start of the long-term accretion from T1 (closest to the river) to T3 (furthest, Figures 6f–6h).

The beach width at La Escobilla decreased from 85 m at T1 to 61 m at T3 (Figure 6d). The backbeach was relatively flat and low at all three transects and only at T1 the slope started to increase some 500 m from the shoreline (Figure 6c). The accommodation space at T1 was determined by the backbeach elevation reaching above 10 m + MSL 546 m behind the beach, although using the IFD would have resulted in a similar accommodation space (≈ 600 m). At T2 and T3, the backbeach profile remained low and the accommodation space was set by the IFD, resulting in 476 m at T2 and only 23 m at T3. This shows the sensitivity of the accommodation space to individual buildings: the backbeach was not highly developed but there are a few houses behind T3, leading to the much lower accommodation space. Moreover, while the accommodation space was higher at T1 and T2, there is a village behind the beach in-between these two transects, leading to significantly less accommodation space there.

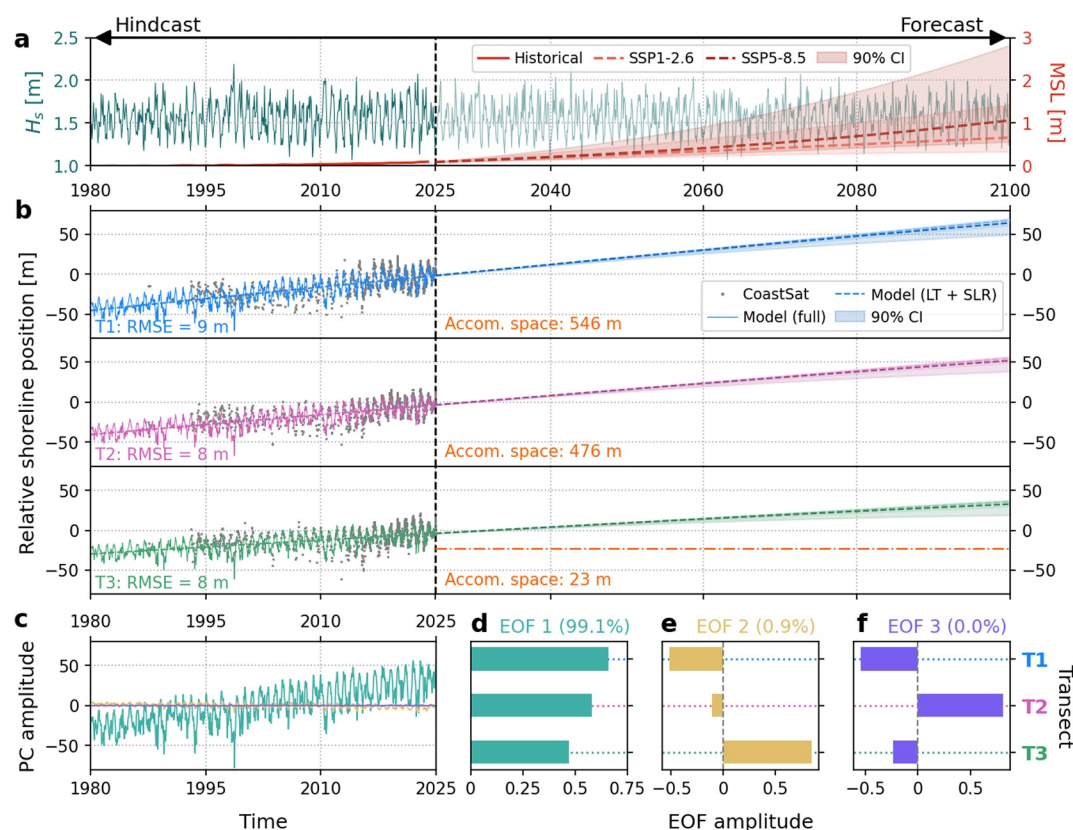


Figure 7. Shoreline modeling results at La Escobilla, Mexico. (a) Wave and sea level time series used to force the model; (b) Modeled shoreline position at each transect for the hindcast (1980–2024) and forecast (2025–2100) periods. Gray dots are the CoastSat shorelines, solid lines represent the full model results, and dashed lines only include the long-term trend (v_t) and sea level rise (SLR) components. In the forecasts, the two dashed lines represent the median SSP1–2.6 (lighter color) and SSP5–8.5 (darker color) SLR projections, while the shading indicates the area between the 5th and 95th percentile; (c) Amplitude of the three PCs over the hindcast period; (d–f) Amplitudes of the three EOFs at each transect and percentage of explained variance.

The model showed similar results for the three transects and generally matched the observations well, replicating the seasonal behavior and long-term accretion with relatively low RMSE values (8–9 m, Figures 7a and 7b). However, it struggled with simulating the amplitude of interannual oscillations, which it underestimated, most evidently at T3. The observed accretion over the past decades was simulated by the model through a linear trend, contrasting with the observed stability in shoreline position between 1990 and 2010 and increased accretion afterward.

The synchronous behavior among the transects was also reflected in the EOF analysis: EOF 1 explained virtually all variance in the signal, representing a cross-shore mode (including the seasonal cycle) as well as the long-term accretion trend, strongest at T1 and weakening slightly to T3 (Figures 7c and 7d). The other two EOF modes were negligible compared to EOF 1 (Figures 7e and 7f). The future projections all showed continued accretion, again strongest at T1 (50+ m by 2100) and weakening toward T3 (15–30 m), even under nearly 3 m of SLR. Differences between the SLR scenarios were small (Figure 7b).

3.3. Global Results

Observed shoreline change and accommodation space varied significantly across the seven other locations (see overview in Table 3; figures analogous to Figures 4–7 are given in Appendix D). Strong and clear seasonal cycles were apparent at João Barrosa (up to 36 m) and Maşīrah Island (up to 27 m). At Alagadi, Busca Vida, Dirk Hartog Island, Tortuguero, and Rancho Nuevo, some seasonality was visible, but inter-annual or long-term signals generally dominated shoreline change over the past decades.

Table 3
Results for All Nine Sea Turtle Nesting Sites Analyzed in This Study

Site	Beach slope	Trend	Beach width	IFD	BBD	Accom. Space
Long Beach, AI	0.1*	Eroding	89–99	114–511	176–526	25–413
Dirk Hartog Is., AU	0.045–0.085	Eroding	45–55	>860	69–483	22–428
Busca Vida, BR	0.085–0.105	Stable	27–35	44–216	>649	17–181
Tortuguero, CR	0.1*	Accreting	37–40	>1000	>1000	>1000
João Barrosa, CV	0.045–0.05	Accreting	35–62	>915	603–899	567–864
Alagadi, CY	0.1*	Eroding	58–73	393–576	121–490	56–417
La Escobilla, MX	0.06–0.065	Accreting	61–85	84–682	>631	23–546
Rancho Nuevo, MX	0.1*	Eroding	21–36	>1000	>1000	>1000
Maşīrah Is., OM	0.065–0.085	Stable	83–136	>1000	301–634	176–498

Note. The beach slope was estimated using CoastSat and was used in the SLR term of the shoreline model. Asterisks denote a default slope of 0.1, used when the slope estimation was not reliable (i.e., do not represent measured beach slope). The distance ranges (final four columns) are given in meters and represent the range across the three transects of each site. In the final three columns, values with a > sign are minimum values (e.g., the transects generally extended 1,000 m landward from the shoreline, so if no infrastructure was within 1,000 m, this is denoted as >1,000).

Several sites showed a long-term historical erosion trend, both in the linear fit based on the CoastSat-derived shoreline positions, as well as in the model trend (v_{lt}). Rancho Nuevo showed the strongest erosion (0.8–0.9 m/year at T3), followed by erosion rates below 0.5 m/year at Long Beach, Dirk Hartog Island, and Alagadi (Figure 8). Busca Vida and Maşīrah Island had relatively stable shorelines, while Tortuguero, La Escobilla, and particularly João Barrosa (up to 2 m/year) showed accretion trends.

Over the forecast period, the model projected significant shoreline retreat at Long Beach, Dirk Hartog Island, Alagadi, and Rancho Nuevo by 2100. At Rancho Nuevo this was well below the available accommodation space, but at Dirk Hartog and Alagadi accommodation space was limited at two of the three transects, suggesting that shoreline retreat at these sites could lead to a reduction in beach width, especially under the SSP5–8.5 scenario. The model generally projected continued accretion at João Barrosa and La Escobilla until 2100. Moreover, João Barrosa, Tortuguero, Rancho Nuevo, and Maşīrah Island had large accommodation space at all three transects.

The difference in shoreline change between the SLR scenarios varied significantly across the nine sites, with higher Bruun coefficients (c) in the model (i.e., more SLR impact) leading to larger differences. The median projections were generally close together, but the 90% confidence intervals spanned wide ranges at some locations. At Maşīrah Island, for instance, the 2100 projection ranged from no change or even slight accretion (SSP1–2.6 5th percentile) to over 50 m of shoreline retreat (SSP5–8.5 95th percentile). For some locations the range

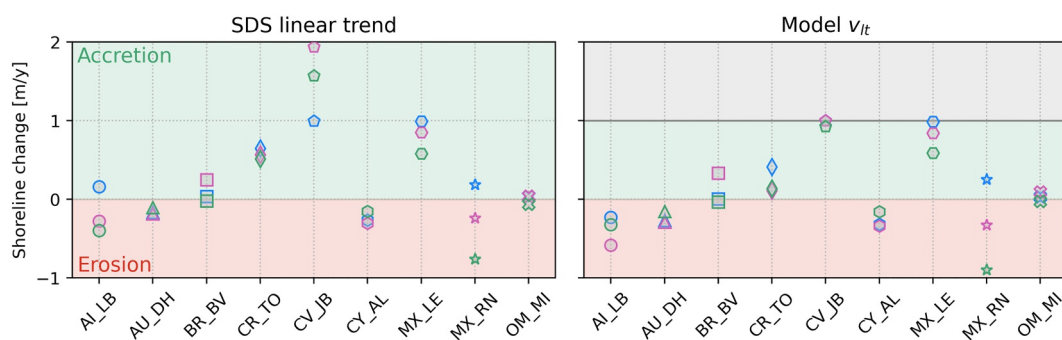


Figure 8. Long-term shoreline position trends at each location and transect based on a linear regression of the smoothed observations (left) and the long-term trend (v_{lt}) in the model (right, bounded between -1 and 1 m/y). Marker shapes denote the site (see x-axis) and marker edge color the transect (T1 blue, T2 pink, T3 green). Sites are abbreviated by Country_Site (e.g., AI_LB = Ascension Island, Long Beach).

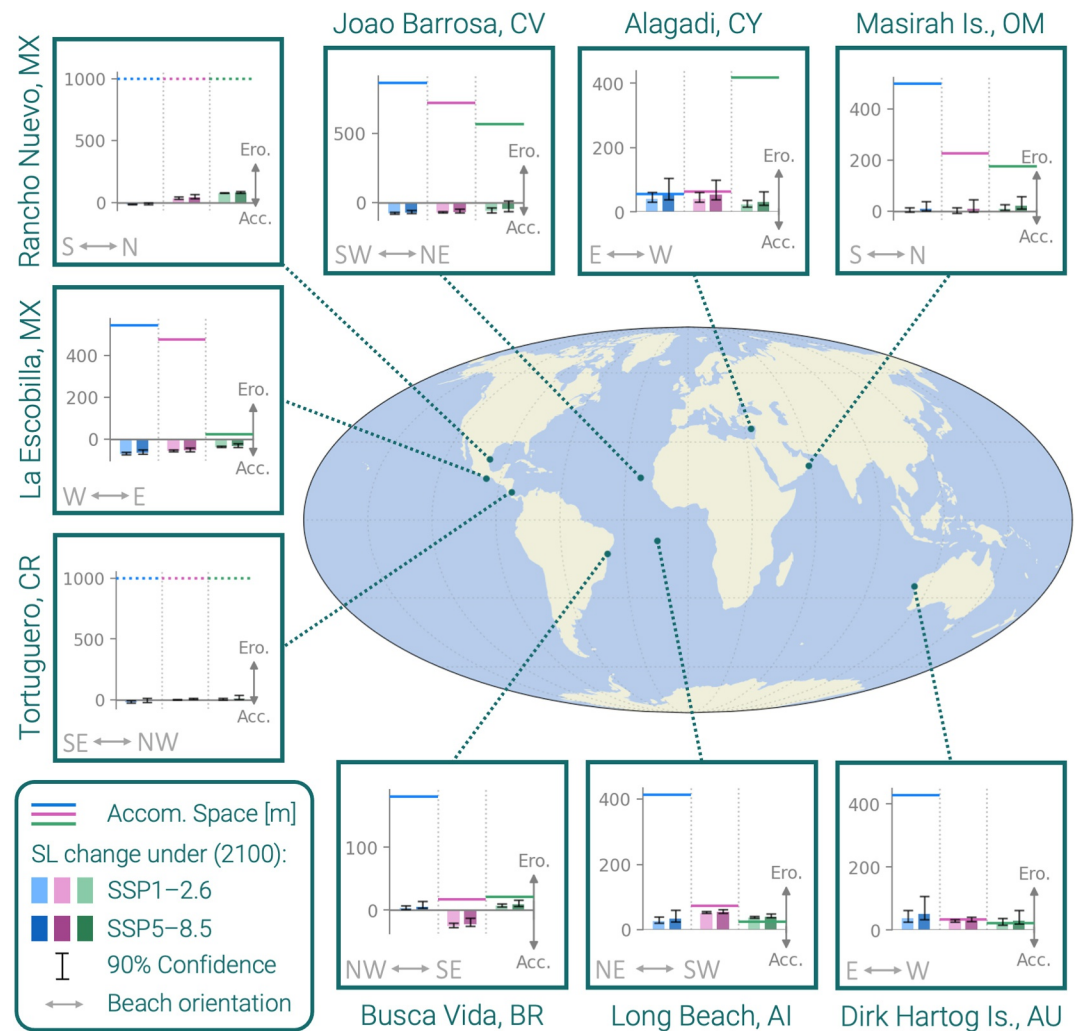


Figure 9. Overview map showing the accommodation space (horizontal lines) and projected shoreline change at the three transects (T1 blue, T2 pink, T3 green) of all nine nesting sites. Projected shoreline change is shown for the two sea level rise (SLR) scenarios (SSP1–2.6 in brighter colors, SSP5–8.5 in darker colors) with the bars representing the median and the error whiskers the 90% SLR confidence interval. Erosion is positive (upward) and accretion is negative (downward) to visualize the effect on the accommodation space. The beach orientation (direction from T1 to T3) is given by the horizontal arrows. The dotted accommodation space lines at Rancho Nuevo and Tortuguero indicate that the accommodation space is at least 1 km.

covered accretion as well as erosion. At other locations, like La Escobilla or Rancho Nuevo, the difference between the scenarios was small compared to the projected change.

4. Discussion

4.1. Vulnerability of Global Nesting Sites to Erosion and SLR

Our results suggest that vulnerability to future erosion and SLR varies significantly across the nine sites, and in alongshore direction at some sites (Figure 9). At seven of the nine sites (all except La Escobilla and João Barrosa), potential future shoreline retreat is projected at one or more of the three transects. At some transects, the projections also include accretion, depending on the SLR scenario (e.g., Tortuguero, Maşrah Is). La Escobilla and João Barrosa are clearly projected to continue accreting in the future, suggesting these sites are the least vulnerable to SLR. Long Beach, Dirk Hartog Is., and Alagadi have limited accommodation space, which is exceeded for several scenarios. This implies that these are the most vulnerable sites, facing potential reduction of beach width and nesting area in the future. At the remaining eroding sites, projected shoreline retreat by 2,100 is below the estimated accommodation space, although close at some transects (e.g., Busca Vida T3, Long Beach T2). These findings

highlight the variability in the morphological evolution and characteristics across global nesting sites and show the importance of understanding these, including the backbeach topography.

While our results provide insights into the future vulnerability of the nine sites, they present significant uncertainties, for example, in the definition of the accommodation space. The IFD is particularly sensitive to building positions in sparsely developed areas, because the position of a single building can strongly influence the available accommodation space. This is evident at La Escobilla where the accommodation space at T3 is much lower than at T1/T2 due to one building (Figure 6d). In general, if the accommodation space is determined by infrastructure, it is not just a question of whether the beach can migrate through, but also whether the infrastructure may be allowed to erode to provide room for the beach system (Lansu et al., 2024). Additionally, here we defined the BBD simply by an elevation of 10 m + msl, but ideally it would account for the backbeach slope to identify cliffs, for instance. However, the horizontal resolution of DeltaDTM (1 arcsec) and other state-of-the-art global elevation models complicates efforts to identify steep slopes because the sample points along the transects are often 40–50 m apart. Local, high resolution assessments of the backbeach elevation and geology could therefore substantially improve accommodation space estimates but are costly and time-intensive.

Our analysis assumes a fully sandy profile in which the entire beach width retreats together with the shoreline until exceeding the accommodation space and the beach starts narrowing. However, the future evolution of the beach will depend on the geomorphology of the profile. For instance, dunes behind the beach will respond more dynamically than hard substrates (Moore et al., 2025). If the beach is underlain by rocky formations, erosion may expose a rocky shoreline that is potentially inaccessible to turtles (Wildermann et al., 2024). Dirk Hartog Island and João Barrosa both exhibit rock formations at some places along the beach. Moreover, at Dirk Hartog Island, the beach is backed by a steep rocky slope. Here, this translated to zero accommodation space, but these slopes may erode and allow some beach migration (Walkden & Dickson, 2008). At Tortuguero and Rancho Nuevo, accommodation space was not limited within the first kilometer from the shoreline, suggesting they can accommodate significant shoreline retreat. But both sites are located on barrier islands, for which the response to SLR might also differ from regular sandy coastlines (Anarde et al., 2024; Moore & Murray, 2022; Thomas et al., 2024). Similarly, coral islands and atolls may exhibit different geophysical compositions and responses to SLR (Cuttler et al., 2020; Garcin et al., 2022; Masselink et al., 2020). Accounting for these different geological settings requires a more complex and integrated modeling approach. For example, shoreline models could be coupled to cliff erosion models to account for a rocky backbeach (Erikson et al., 2017; Walkden & Dickson, 2008; Wolinsky & Murray, 2009).

4.2. Model Performance, Limitations, and Uncertainty

Model performance varies considerably across sites and transects (Figure 10) but aligns with previous shoreline modeling efforts reported in the literature, even at well-monitored sites (e.g., Gomez-de la Peña et al., 2023; Montaña et al., 2020; Repina et al., 2025). Both performance metrics show agreement in their results (i.e., locations scoring high on the Taylor diagram also score high with Mielke's index). The obtained λ indices (Figure 10a) are similar to those in a previous blind-testing study of shoreline models (Montaña et al., 2020). At many sites, the model captures the seasonal dynamics, but struggles to replicate inter-annual or longer-term trends not directly linked to wave conditions or sea level changes. Moreover, the Taylor diagram shows that the model generally underestimates the variability in the observations (Figure 10b). These are both common limitations of reduced complexity models (Bosboom et al., 2014; Hunt et al., 2023; Vitousek, Vos, et al., 2023). This results in lower performance at sites where interannual to long-term oscillations dominate the shoreline signal (e.g., Alagadi, Busca Vida, and Dirk Hartog Island), whereas the model performs better where wave-related seasonal shoreline cycles dominate (e.g., La Escobilla and Maşīrah Island). Notably, La Escobilla shows high performance metrics even though the model cannot replicate the interannual variation in the accretion (instead modeling it through the linear trend term, Figure 7). At some sites, performance varies significantly across transects (e.g., Long Beach and João Barrosa), which is also common in shoreline modeling, especially at embayed beaches (Abdulsalam et al., 2025; Repina et al., 2025).

The model has several limitations, which can partly explain why it struggles at locations such as Long Beach T1. First, the cross-shore term is hard-wired to erode the shoreline with increasing wave energy and therefore cannot replicate accretion during the high-energy season, which happens at T1 during the seasonal rotation at Long Beach. Consequently, the model minimizes the cross-shore contribution and tries to replicate the behavior with

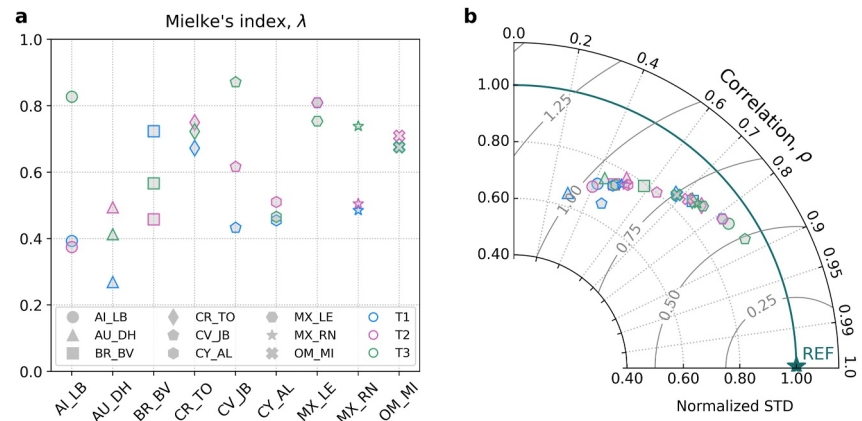


Figure 10. Model performance across the sites (marker shape) and transects (edge color), assessed through (a) Mielke's index (λ); and (b) a Taylor diagram, which shows the Pearson correlation (ρ , angle), normalized standard deviation (radial axis), and normalized RMSE (contours). The latter two are normalized by the standard deviation of the observations, hence a perfect model would have $nSTD = 1$, $\rho = 1$ and $nRMSE = 0$, corresponding to the star marked REF. Sites are abbreviated by Country_Site (e.g., AI_LB = Ascension Island, Long Beach).

longshore transport only. Second, the version of CoSMoS-COAST used here computes the longshore transport differently than in the original one-line formulation (Equation 2). This allows each transect to be modeled independently but does not enforce sediment continuity between neighboring transects. In other words, although longshore transport processes are represented within the model, alongshore sediment exchange is not dynamically coupled across transects. Third, due to forcing the model with offshore wave conditions, the waves are rotated such that the mean direction is shore-normal. This is a partly valid assumption as oblique waves generally refract toward the coast (Holthuijsen, 2007); however, this assumption may not always hold. Long Beach is situated on the northwest side of Ascension Island, while the dominant wave direction is from the south-east (trade wind swells), essentially coming from behind the island and potentially not fully refracting to normal incidence.

A key limitation for this study is the model's long-term components, which aligns with many previous studies (e.g., Le Cozannet et al., 2019; Vitousek et al., 2024). While seasonal fluctuations are evident in the data and may be inferred from the forcing conditions, historical SLR has been low ($\mathcal{O}(10\text{--}15\text{ cm})$ since 1980), making the morphological response hard to distinguish from shorter-term “noise” (Vitousek, Barnard, & Limber, 2017). Nevertheless, sea level has risen at all nine sites, which the model is hardwired to translate to shoreline retreat (Bruun rule). At eroding (accreting) transects, the model optimization generally tends to maximize (minimize) the Bruun coefficient (c), which effectively modulates the selected transgression slope. In our model runs, the optimized value for c reaches the upper or lower bound for all transects (Figure C1), also showing the uncertainty in the applied transgression slopes. At accreting transects, the minimal SLR term combined with a positive linear trend (v_{lt} , replicating the accretion) generally projects continued accretion in the future (most obvious at La Escobilla and João Barrosa). While possible, it is uncertain whether the underlying causes will maintain accretion over time. Moreover, while the v_{lt} term allows the model to partially replicate non-wave/sea level-driven processes, it is dependent on the accuracy and consistency of the historical observations from which it is derived. Especially in the early part of the hindcast, there are relatively few observations. v_{lt} is therefore very sensitive to bias or extreme values in these early observations (e.g., if early observations are predominantly from the same season, this may bias v_{lt}). Moreover, it cannot account for long-term variability in sediment sinks and/or sources.

Next to uncertainty arising from the model itself, there is also intrinsic uncertainty in the natural processes. While the included uncertainty in SLR projections is not trivial, the chosen transgression slope generally has a much stronger effect on the projected shoreline change (Antolínez et al., 2019; Vitousek et al., 2024; Wolinsky & Murray, 2009). Although the Bruun coefficient (c) allows some modulation of the transgression slope during model optimization, future studies could explore a set of potential transgression slopes more rigorously (e.g., Vitousek et al., 2024).

Finally, in the forecast, we opted to focus on sea level driven shoreline change and neglected expected future changes to the wave climate (Morim et al., 2019; Reguero et al., 2019) and storm intensity and frequency (Morim

et al., 2025; Sobel et al., 2016), which could lead to changes in sediment transport patterns at the nine sites. Based on global projections, sites with potentially more pronounced changes in future wave height and period include La Escobilla (increase), Alagadi (decrease), and João Barrosa (decrease; Morim et al., 2019; Morim et al., 2020). However, the impact of such changes on shoreline dynamics are site-specific and uncertain and were therefore not considered in this study. The monthly reshuffling of the historical ERA5 wave time series for the projections (Section 2.3) also mean that interannual variability in wave climate is removed.

These uncertainties related to satellite-derived shoreline extraction, wave and sea level forcing, and parameter calibration introduce uncertainty in the exact magnitude of projected shoreline changes. However, they are largely systematic across sites and scenarios. Therefore, we do not expect them to substantially affect the comparative assessment of which nesting beaches are more or less vulnerable to future erosion. In other words, while absolute projections should be interpreted with caution, the relative vulnerability rankings presented here are considered robust for comparative and pre-screening purposes.

4.3. Implications for Conservation and Beach Management

Due to the inherent uncertainty in our long-term predictions, they should be used cautiously to help inform management decisions. Accordingly, our modeling framework represents a comparative, first-order tool to assess relative vulnerability among nesting beaches, rather than a source of precise deterministic shoreline forecasts. Uncertainty notwithstanding, the projected erosion at Dirk Hartog Is., Alagadi, and Long Beach is concerning because these sites show shoreline erosion trends and have limited accommodation space that may lead to loss of nesting habitat. Future studies should carry out more detailed assessments of these sites, which may help inform decision-makers on beach management and/or conservation measures. Such assessments could include local, higher resolution data on beach and backbeach characteristics and more sophisticated coastal resilience indicators, beyond the shoreline position (e.g., Dong et al., 2018). They should also include more rigorous quantification of model and wave climate uncertainty (Kroon et al., 2025; Vitousek et al., 2021; Zarifsanayei et al., 2023).

Our results also reveal dominant modes of shoreline change at the different sites, which may be important for assessing the vulnerability to future erosion and suitability of potential beach management strategies. For instance, if, as we hypothesize, the river at La Escobilla is responsible for the observed accretion, then an effective measure protecting the beach from erosion might be to simply leave the river be—i.e., not modify its course or interrupt the sediment supply through damming. This highlights the variety of processes that may affect coastal change and the need to understand these in vulnerability assessments.

The large variability in projected shoreline change demonstrates that the bathtub approach used in many previous studies (e.g., Beber et al., 2024; Fish et al., 2005; Fuentes et al., 2010; Rivas et al., 2023; Varela et al., 2019) is not suitable to assess SLR vulnerability at nesting beaches. Under the bathtub assumption, any rise in sea level automatically translates to shoreline retreat and reduction of beach width, as the static morphology rules out stable or accreting profiles. The loss of nesting habitat is then purely a function of the elevation of the current nesting zone. Applying this approach to the nesting sites here would therefore have resulted in projected erosion and habitat loss at all nine sites, regardless of historical and present shoreline evolution patterns.

For example, a bathtub approach applied at La Escobilla over the past 30 yrs under a realistic SLR scenario (± 20 cm) would have implied shoreline retreat proportional to the local beach slope. Instead, our study revealed that the shoreline has progressed by about 20–30 m over this timespan. Similar tendencies for static approaches to overestimate coastal exposure and vulnerability relative to dynamic or process-based methods have been documented in previous studies (Khojasteh et al., 2021; López-Dóriga & Jiménez, 2020; Passeri et al., 2015; Rogers et al., 2012). Therefore, our results indicate that using the bathtub approach presents significant problems in addressing future SLR vulnerability assessments of sea turtle nesting beaches.

In this study, vulnerability is assessed in terms of physical habitat availability, represented by the beach width. While physical availability is a necessary prerequisite for successful nesting, it does not directly equate to habitat quality, accessibility, or realized nesting success, which are influenced by species-specific traits, nesting behavior, and local management context (Garcin et al., 2022; Martins et al., 2022; Stokes et al., 2024). For example, some populations may tolerate substantial narrowing of the beach through behavioral plasticity or nesting site selection, whereas others may be more sensitive to reductions in beach width or increased inundation risk (e.g., Cassill, 2021; Laloë & Hays, 2023). As such, the physical vulnerability metrics presented here should

be interpreted as first-order constraints on nesting habitat, providing a foundation for integrating ecological sensitivity and management factors in future, site-specific assessments. Accordingly, our modeling framework represents a large-scale, first-order pre-screening tool to help orient protection, management, or restoration priorities, rather than a stand-alone method for site-specific management decisions.

Due to the global-scale coverage of the data sets used herein, our approach is readily transferable to assess shoreline evolution and potential vulnerability at other sites around the world, though it is mainly suitable for relatively open coasts and embayed beaches. Morphologically more complex sites, including river mouths, basin inlets, or migrating sand spits, may require more advanced modeling approaches to quantify beach change because the shoreline position may not provide sufficient information (French et al., 2016; Murray et al., 2014). For instance, the olive ridley mass nesting sites in Odisha, India (Shanker et al., 2004) and the leatherback (*Dermochelys coriacea*) rookeries at Braamspunt, Suriname and Awala-Yalimapo, French Guiana (Fossette et al., 2008) are situated near large river mouths and dynamic sand spits, which can change shape rapidly, on timescales ranging from months to a few years. In such environments, shorelines determined using transect-based methods could overlap or intersect due to complex spit formation and shifting sandbanks. Moreover, shoreline recession does not necessarily indicate beach narrowing or habitat loss, but can instead reflect spit elongation or morphological reconfiguration occurring over these shorter timescales.

5. Conclusion

In this paper, we combined CoastSat-derived shorelines, shoreline modeling (CoSMoS-COAST), and global data sets to analyze the shoreline evolution, characteristics, and future vulnerability of nine globally important sea turtle nesting beaches. We identified seasonal and long-term trends in shoreline position and used the shoreline model CoSMoS-COAST (Vitousek, Vos, et al., 2023) to hindcast daily shoreline positions from 1980 to 2024 and forecast them from 2025 to 2100 under two SLR scenarios, including associated uncertainty. Additionally, we quantified the available accommodation space at each site using a global digital terrain model (DeltaDTM; Pronk et al., 2024) and global infrastructure footprints (Overture maps). Long-term shoreline evolution and seasonality varied considerably across the nine sites, with four sites showing erosion trends and three sites accretion. The future shoreline projections indicated that one-third of the sites may be particularly vulnerable to SLR, due to projected shoreline retreat coupled with limited accommodation space. Our results (a) help understand the seasonal and long-term morphodynamics at these critical nesting beaches, (b) indicate which sites may be vulnerable to future erosion and SLR, and (c) provide a readily transferable framework to analyze shoreline evolution and vulnerability at nesting sites around the world. Given the identified uncertainties in our analysis, future work might conduct more detailed assessments at vulnerable sites, including local-scale data and robust uncertainty quantification, to support effective conservation planning and targeted management strategies.

Appendix A: Description of Remaining Study Sites

Below is a description of the seven study sites that were not described in detail in the main text.

A1. Dirk Hartog Island, Australia (AU_DH)

Dirk Hartog Island is a large, remote island on the central west Australian coastline, which hosts an important regional loggerhead turtle (*Caretta caretta*, *Cc*) rookery (Prince, 1994). Nesting occurs from November to April and is concentrated at Turtle Bay on the northern tip of the island, spanning five relatively narrow beaches (2.1 km total length, about 30 m wide) interspersed with rocky sections and backed by steep rocky slopes (Reinhold & Whiting, 2014). Though the island is exposed to high wave energy ($\bar{H}_s \approx 2$ m), Turtle Bay is partly sheltered from the predominantly south-westerly swell. Nonetheless, during cyclones, entire nesting beaches have been stripped of sand (Reinhold & Whiting, 2014). The tidal range is relatively small (0.9 m).

A2. Busca Vida, Brazil (BR_BV)

Busca Vida is situated on the northern outskirts of the city of Salvador in Bahia, Brazil. Bahia's northern coastline (covering a stretch of about 200 km) is Brazil's primary nesting area of Hawksbill turtles (*Eretmochelys imbricata*, *Ei*; Marcovaldi et al., 1999), while also supporting nesting by green, loggerhead, olive ridley, and

leatherback (*Dermochelys coriacea*, *Dc*) turtles. The shoreline is mostly sandy with interspersed rock and reef formations along the coast (Marcovaldi et al., 2007). The beach at Busca Vida is backed by residential homes and coconut plantations, while there is a river mouth at the southern end. The tidal range (1.7 m) and wave energy ($\bar{H}_s \approx 1.1$ m) are moderate.

A3. Tortuguero, Costa Rica (CR_TO)

Tortuguero National Park covers a 30-km stretch of open beach on the northern Caribbean coast of Costa Rica. This barrier island hosts the largest green turtle rookery in the Atlantic Ocean, holding enormous conservation value for the species (Bjorndal et al., 1999). Nesting occurs between June and November (Restrepo et al., 2023). The relatively narrow beach (≈ 30 m) consists of dark sand and is backed by dense vegetation. The tidal range is very small (0.3 m), and wave energy is moderate ($\bar{H}_s \approx 0.9$ m).

A4. João Barrosa, Cape Verde (CV_JB)

João Barrosa covers a roughly 8 km-long stretch of sandy coast on the southeastern part of Boa Vista island, Cape Verde. The island hosts the largest loggerhead turtle rookery of the endangered eastern Atlantic population, most of which nest near João Barrosa (Marco et al., 2012). The area has a mixed setting of open and embayed beaches backed by sparse vegetation and virtually no human infrastructure. The tidal range is relatively small (0.7 m) but the beaches are exposed to moderate to high wave energy ($\bar{H}_s \approx 1.4$ m).

A5. Alagadi, Cyprus, (CY_AL)

Alagadi covers two pocket beaches on the north coast of Cyprus in the eastern Mediterranean. The two beaches (total length 1.7 km) serve as important nesting habitat for the Mediterranean loggerhead and green turtle populations, which both nest between May and October (Broderick et al., 2002). The region is characterized by a very small tidal range (0.3 m) and relatively low wave energy ($\bar{H}_s \approx 0.8$ m).

A6. Rancho Nuevo, Mexico (MX_RN)

Rancho Nuevo, a stretch of undeveloped open sandy beach along Mexico's northern Gulf of Mexico coast, is the single most important nesting site for the critically endangered Kemp's ridley sea turtle (*Lepidochelys kempii*, *Lk*; Bevan et al., 2014; Shaver & Caillouet, 2015). Kemp's ridleys nest here in mass-nesting events (*arribadas*) from April through July. The beach is relatively narrow (20–30 m) and interspersed by several small rivers and lagoons. The tidal range is very small (0.4 m) and wave energy is moderate ($\bar{H}_s \approx 1$ m).

A7. Maşīrah Island, Oman (OM_MI)

Maşīrah Island is a large island off the eastern coast of Oman, which hosts the second-largest loggerhead nesting population in the world (after the south-eastern US; Willson et al., 2020). It holds huge conservation value for the species, as the North–West Indian Ocean population is classified as *critically endangered* by the IUCN (Casale & Tucker, 2017). The island also hosts smaller nesting populations of green, hawksbill, and olive ridley turtles. The region is strongly influenced by the seasonal Monsoon climate, which overlaps with the nesting season from May through September, bringing high waves. Outside the Monsoon, waves are small leading to a moderate mean wave climate ($\bar{H}_s \approx 1.1$ m). The tide range is relatively high (2 m).

Appendix B: CoastSat Settings

Table B1 gives an overview of the total number of satellite images used per site (before all filtering) and the full manual settings used for the CoastSat analysis. For a complete explanation of all settings we refer to Vos, Splinter, et al. (2019). Briefly, `output_epsg` is the EPSG code of the coordinate reference system to be used at each site; `max_dist_ref` is the maximum distance (m) to the user-defined reference shoreline for a detected shoreline to be valid; `dist_clouds` is the distance (m) around identified clouds, where no shoreline can be mapped; `sand_color` denotes which classifier should be used, based on the beach sand color; `cloud_mask_issue` is a flag that can be

Table B1
Overview of Manually Adjusted CoastSat Settings. All Settings Not Represented in the Columns Were Left at the Default Values (See Vos, Splinter, et al., 2019). Values in the Table Marked With an Asterisk Also Denote Default Values

Site	# of images	output_epsg	max_dist_ref	dist_clouds	sand_color	cloud_mask_issue	s2cloudless_prob
AI_LB	550	32,728	50	100	default*	False*	40
AU_DH	2332	7,849	75	30	default*	True	60
BR_BV	953	31,984	100*	90	default*	False*	30*
CR_TO	594	5,456	100*	90	default*	True	40
CV_JB	637	4,826	75	90	default*	True	30*
CY_AL	2364	6,312	50	90	default*	False*	30*
MX_LE	1063	6,372	100*	90	default*	True	30*
MX_RN	964	6,372	75	90	default*	True	50
OM_MI	1166	32,640	100*	90	bright	True	60

activated in case sand pixels are wrongly identified as clouds on S2 images; and s2cloudless_prob denotes the threshold to identify cloudy pixels in the s2cloudless algorithm for S2 images.

Appendix C: Model Parameters and Optimization

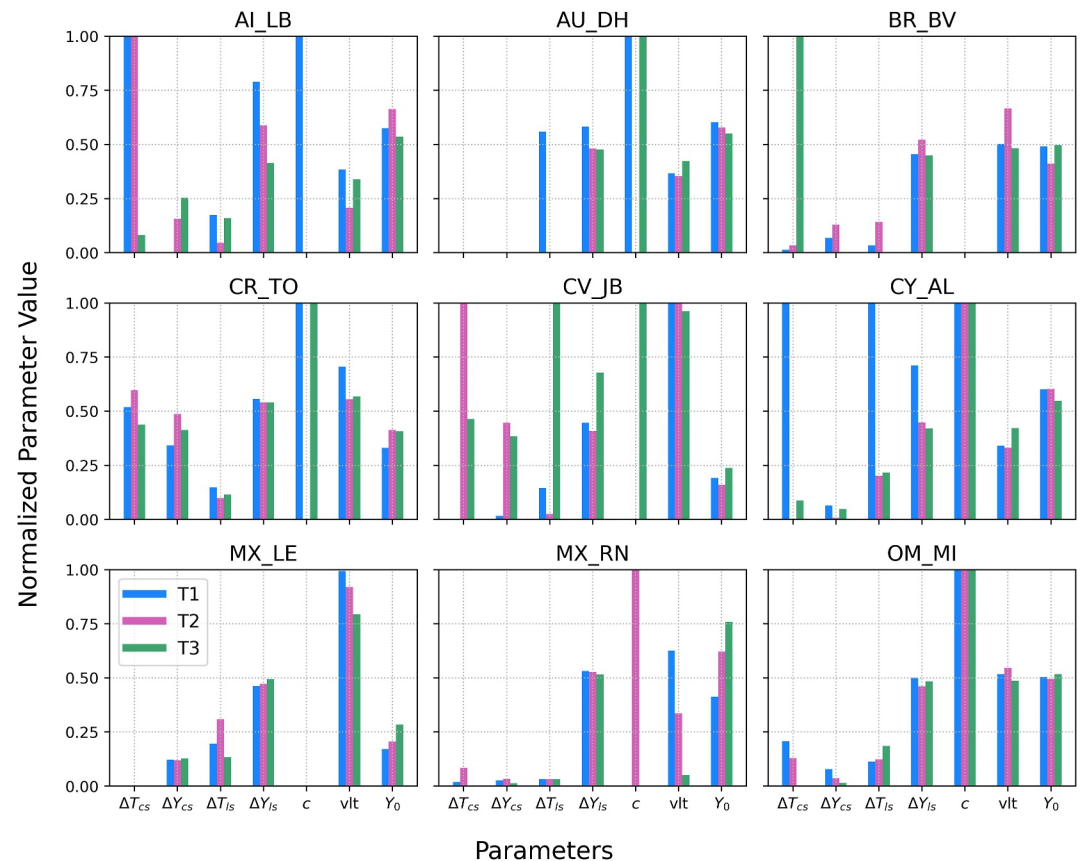


Figure C1. Optimized model parameters for each location and transect. The parameter values are normalized, so the minimum/maximum values in the possible range are represented by 0 and 1 (see Table 2 for the ranges). The ranges of ΔY_{ls} , v_{lt} , and Y_0 are centered around 0, meaning that a value of 0.5 in the bar plots corresponds to 0, higher is positive, and lower is negative.

Appendix D: Observation and Model Results for Remaining Study Sites

Here we present the equivalent to Figures 4–7 for the seven remaining study sites.

Figure D1

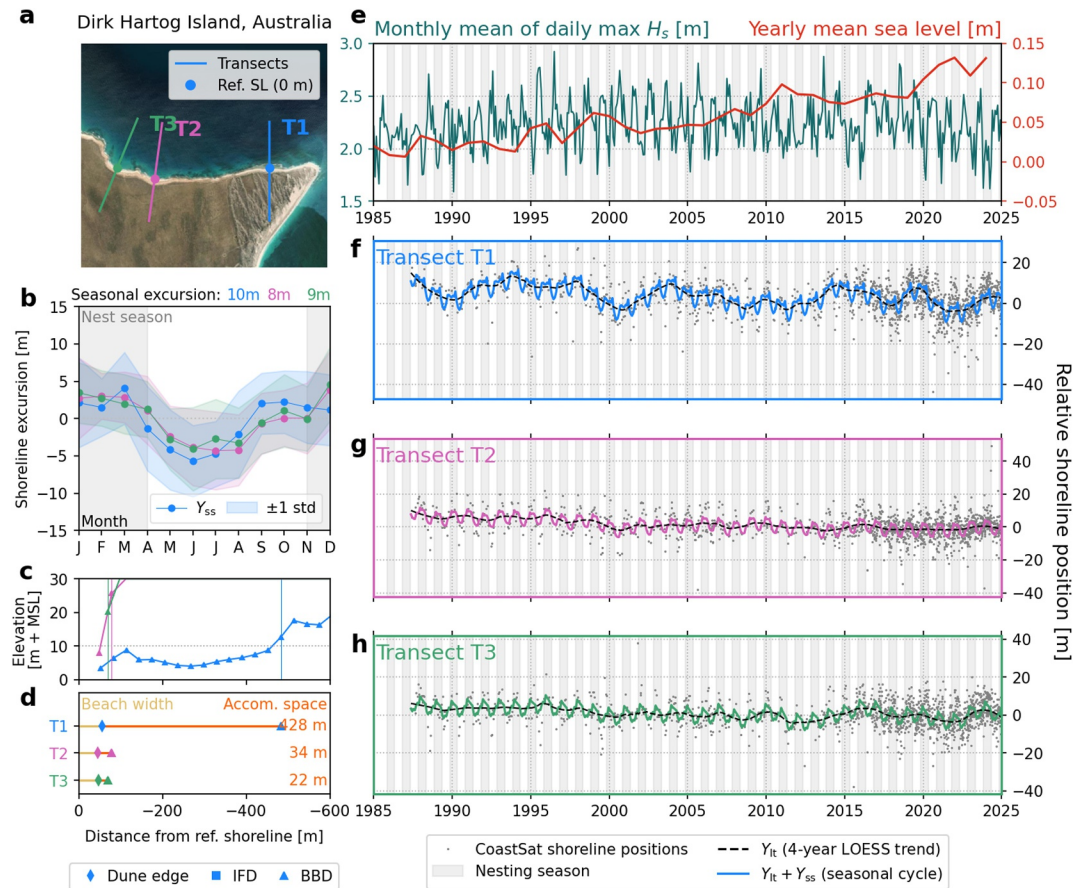


Figure D1. Shoreline and accommodation space analysis for Dirk Hartog Island, Australia: (a) Satellite image showing the transects and reference shoreline position (Ref. SL); (b) Seasonal shoreline component, Y_{ss} , at each transect; (c) Backbeach elevation profiles, with vertical lines denoting the first point above 10 m + MSL; (d) Beach width and accommodation space at each transect; (e) Historical wave and water level time series; (f, g) Observed and decomposed (long-term and seasonal) shoreline position time series at each transect.

Figure D2

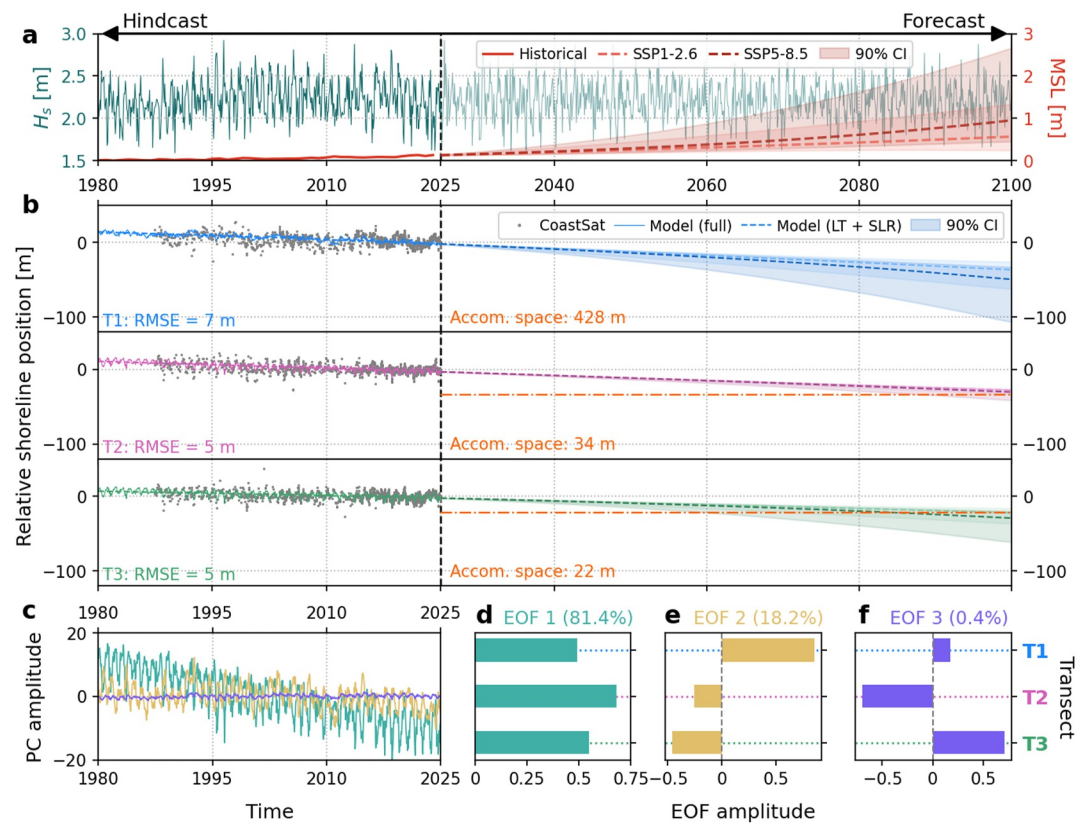


Figure D2. Shoreline modeling results at Dirk Hartog Island, Australia. (a) Wave and sea level time series used to force the model; (b) Modeled shoreline position at each transect for the hindcast (1980–2025) and forecast (2025–2100) periods. Gray dots are the CoastSat shorelines, solid lines represent the full model results, and dashed lines only include the long-term trend (v_{lt}) and sea level rise (SLR) components. In the forecasts, the two dashed lines represent the median SSP1–2.6 (lighter color) and SSP5–8.5 (darker color) SLR projections, while the shading indicates the area between the 5th and 95th percentile; (c) Amplitude of the three PCs over the hindcast period; (d)–(f) Amplitudes of the three EOFs at each transect and percentage of explained variance.

Figure D3

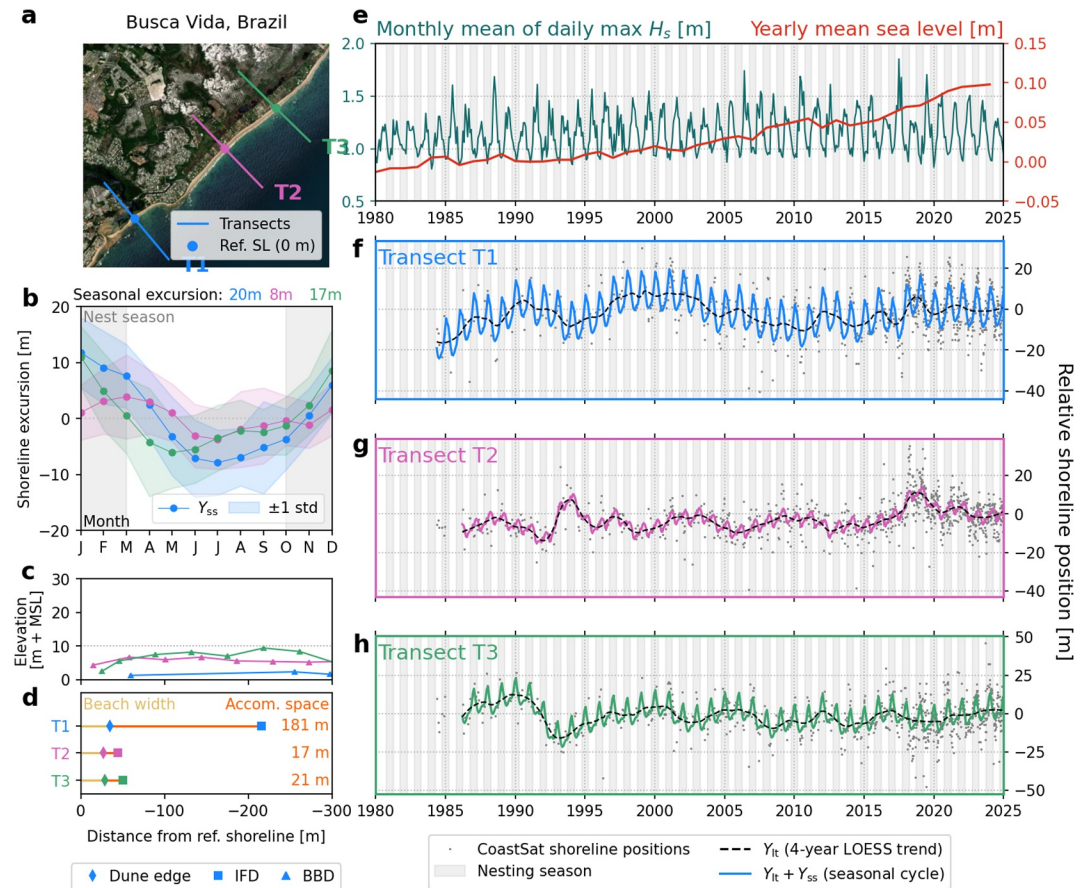


Figure D3. Shoreline and accommodation space analysis for Busca Vida, Brazil: (a) Satellite image showing the transects and reference shoreline position (Ref. SL); (b) Seasonal shoreline component, Y_{ss} , at each transect; (c) Backbeach elevation profiles, with vertical lines denoting the first point above 10 m + MSL; (d) Beach width and accommodation space at each transect; (e) Historical wave and water level time series; (f, g) Observed and decomposed (long-term and seasonal) shoreline position time series at each transect.

Figure D4

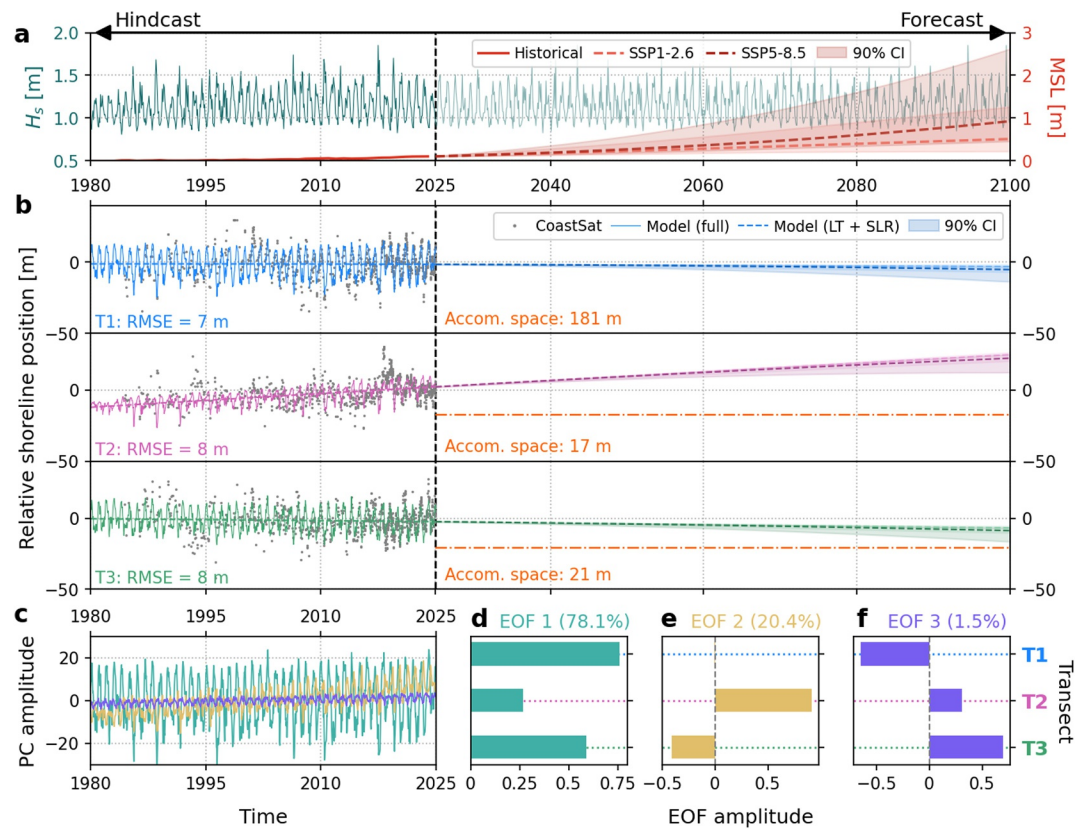


Figure D4. Shoreline modeling results at Busca Vida, Brazil. (a) Wave and sea level time series used to force the model; (b) Modeled shoreline position at each transect for the hindcast (1980–2025) and forecast (2025–2100) periods. Gray dots are the CoastSat shorelines, solid lines represent the full model results, and dashed lines only include the long-term trend (v_{lt}) and sea level rise (SLR) components. In the forecasts, the two dashed lines represent the median SSP1–2.6 (lighter color) and SSP5–8.5 (darker color) SLR projections, while the shading indicates the area between the 5th and 95th percentile; (c) Amplitude of the three PCs over the hindcast period; (d–f) Amplitudes of the three EOFs at each transect and percentage of explained variance.

Figure D5

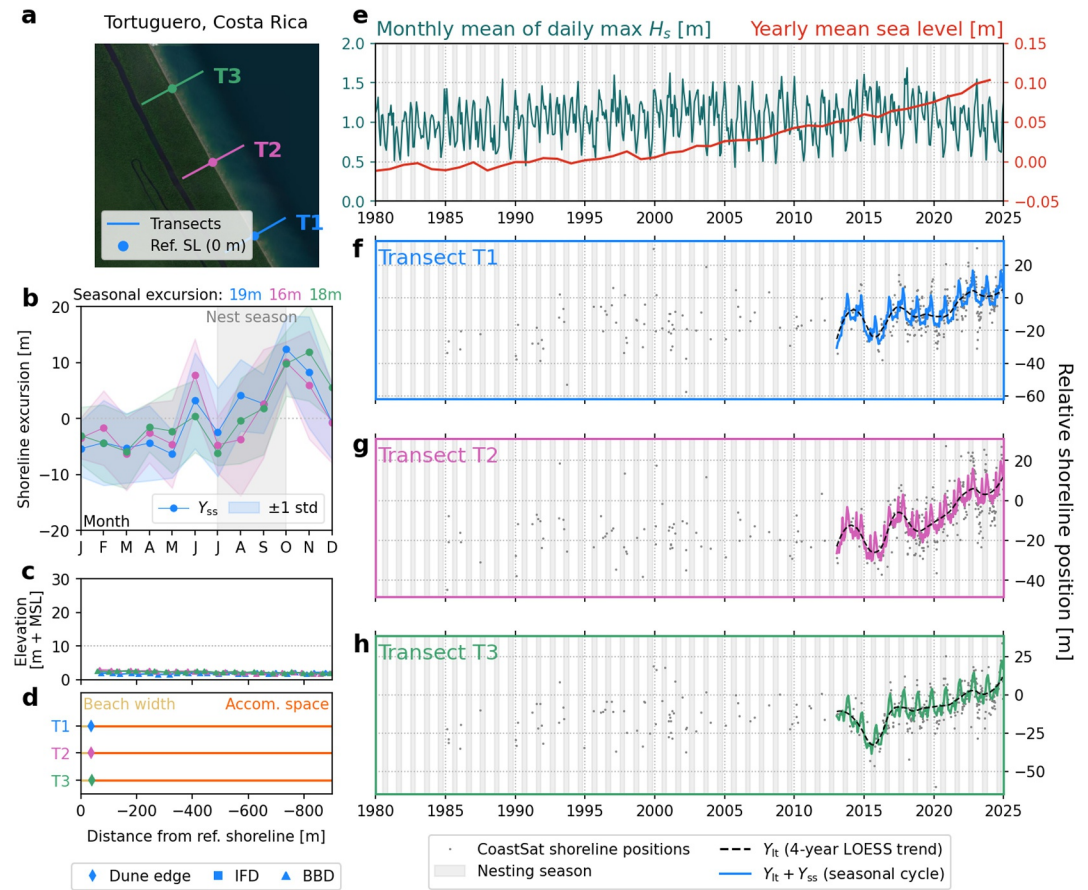


Figure D5. Shoreline and accommodation space analysis for Tortuguero, Costa Rica: (a) Satellite image showing the transects and reference shoreline position (Ref. SL); (b) Seasonal shoreline component, Y_{ss} , at each transect; (c) Backbeach elevation profiles, with vertical lines denoting the first point above 10 m + MSL; (d) Beach width and accommodation space at each transect; (e) Historical wave and water level time series; (f, g) Observed and decomposed (long-term and seasonal) shoreline position time series at each transect.

Figure D6

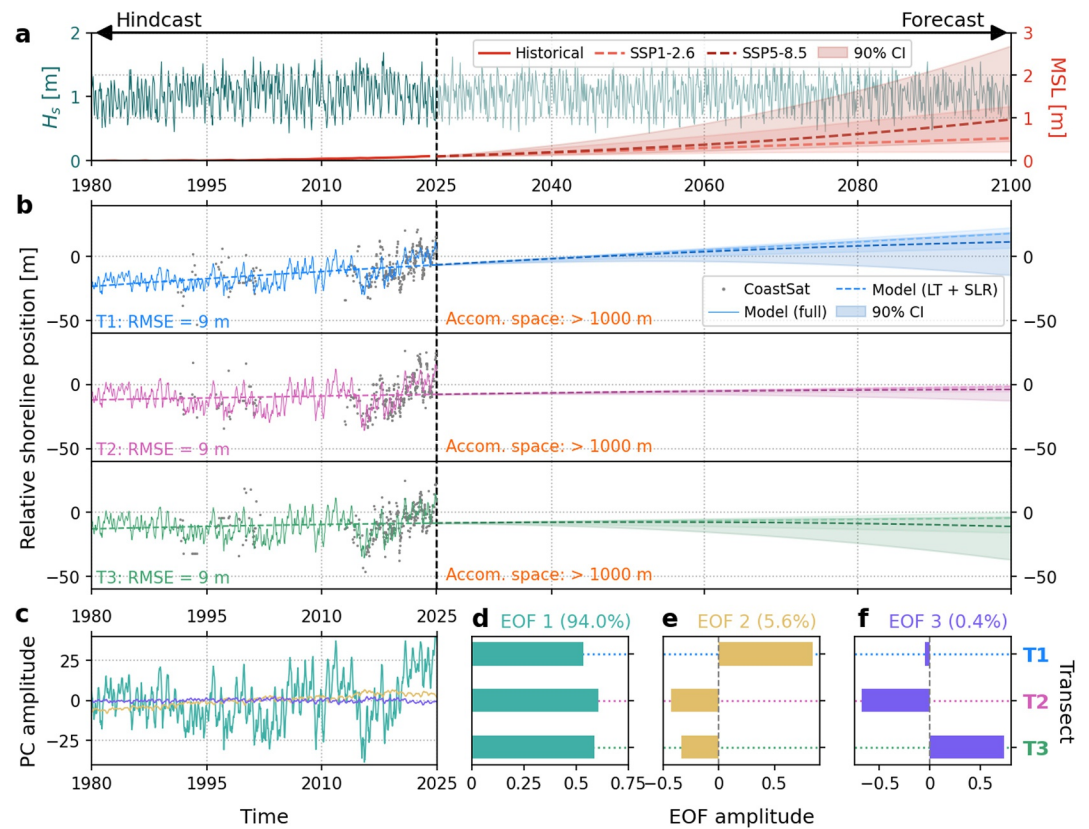


Figure D6. Shoreline modeling results at Tortuguero, Costa Rica. (a) Wave and sea level time series used to force the model; (b) Modeled shoreline position at each transect for the hindcast (1980–2025) and forecast (2025–2100) periods. Gray dots are the CoastSat shorelines, solid lines represent the full model results, and dashed lines only include the long-term trend (v_{lt}) and sea level rise (SLR) components. In the forecasts, the two dashed lines represent the median SSP1–2.6 (lighter color) and SSP5–8.5 (darker color) SLR projections, while the shading indicates the area between the 5th and 95th percentile; (c) Amplitude of the three PCs over the hindcast period; (d–f) Amplitudes of the three EOFs at each transect and percentage of explained variance.

Figure D7

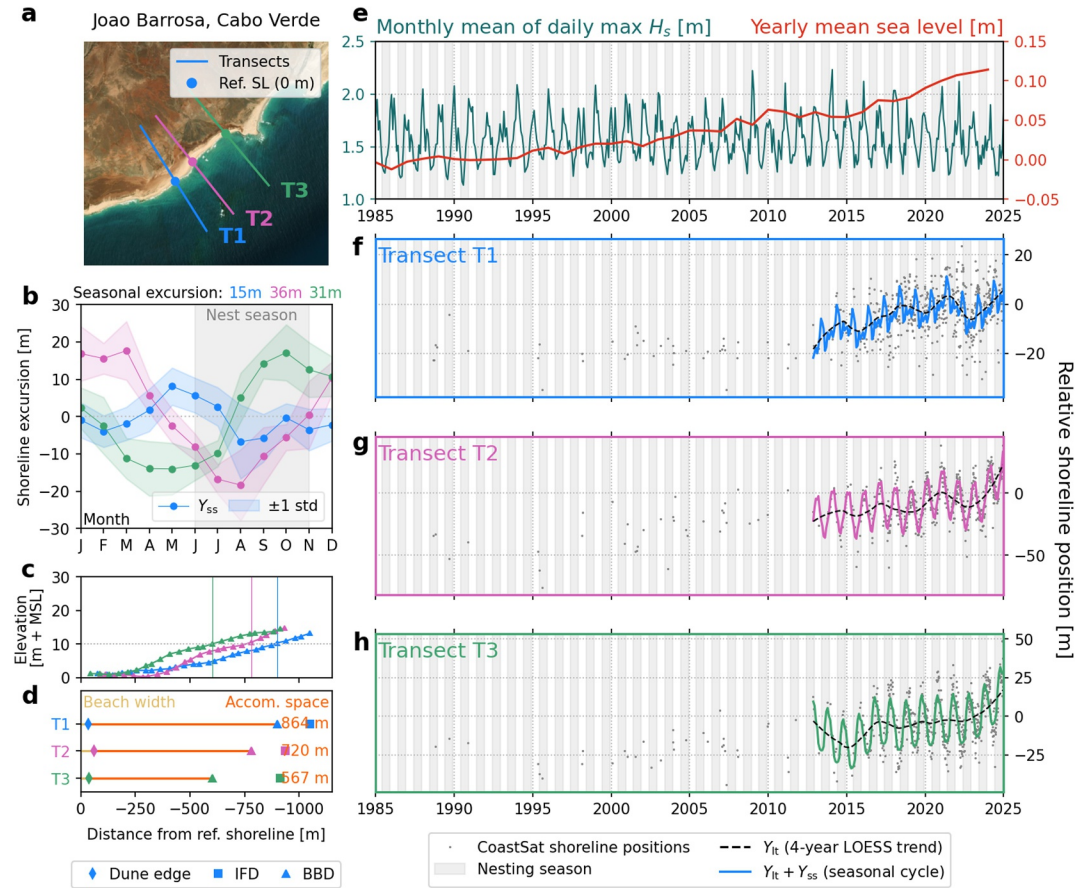


Figure D7. Shoreline and accommodation space analysis for João Barrosa, Cape Verde: (a) Satellite image showing the transects and reference shoreline position (Ref. SL); (b) Seasonal shoreline component, Y_{ss} , at each transect; (c) Backbeach elevation profiles, with vertical lines denoting the first point above 10 m + MSL; (d) Beach width and accommodation space at each transect; (e) Historical wave and water level time series; (f, g) Observed and decomposed (long-term and seasonal) shoreline position time series at each transect.

Figure D8

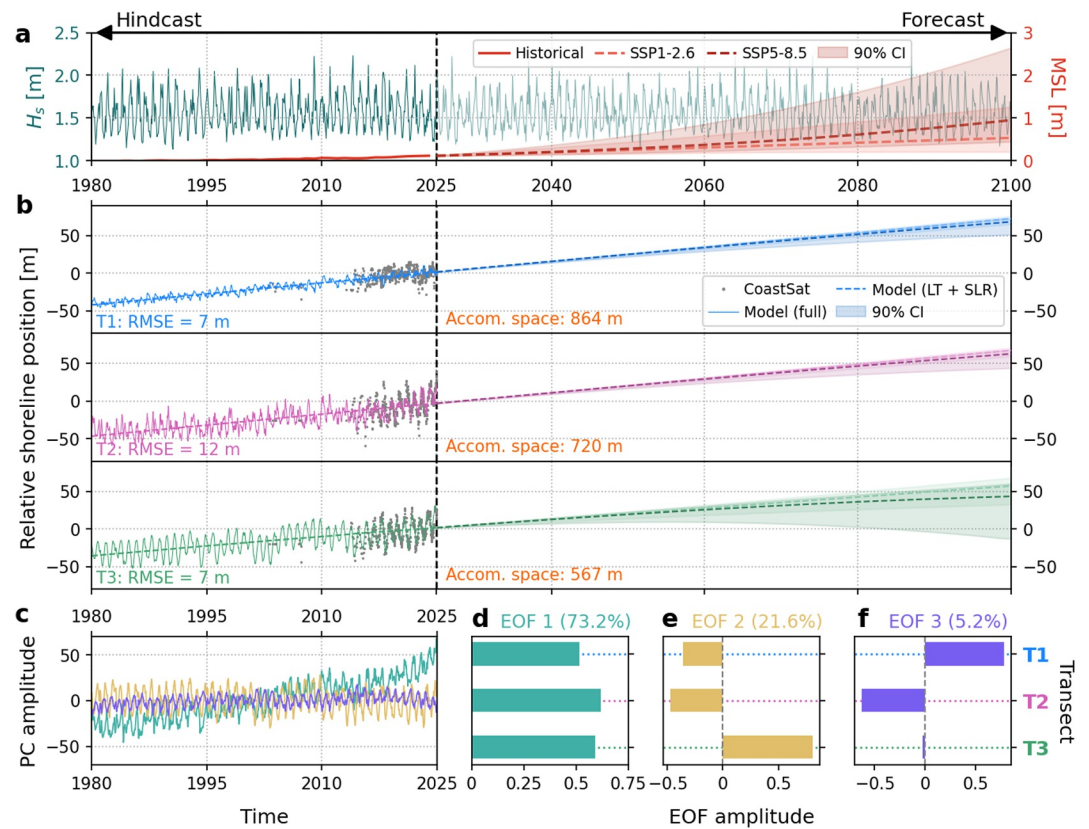


Figure D8. Shoreline modeling results at João Barrosa, Cape Verde. (a) Wave and sea level time series used to force the model; (b) Modeled shoreline position at each transect for the hindcast (1980–2025) and forecast (2025–2100) periods. Gray dots are the CoastSat shorelines, solid lines represent the full model results, and dashed lines only include the long-term trend (v_{lt}) and sea level rise (SLR) components. In the forecasts, the two dashed lines represent the median SSP1–2.6 (lighter color) and SSP5–8.5 (darker color) SLR projections, while the shading indicates the area between the 5th and 95th percentile; (c) Amplitude of the three PCs over the hindcast period; (d–f) Amplitudes of the three EOFs at each transect and percentage of explained variance.

Figure D9

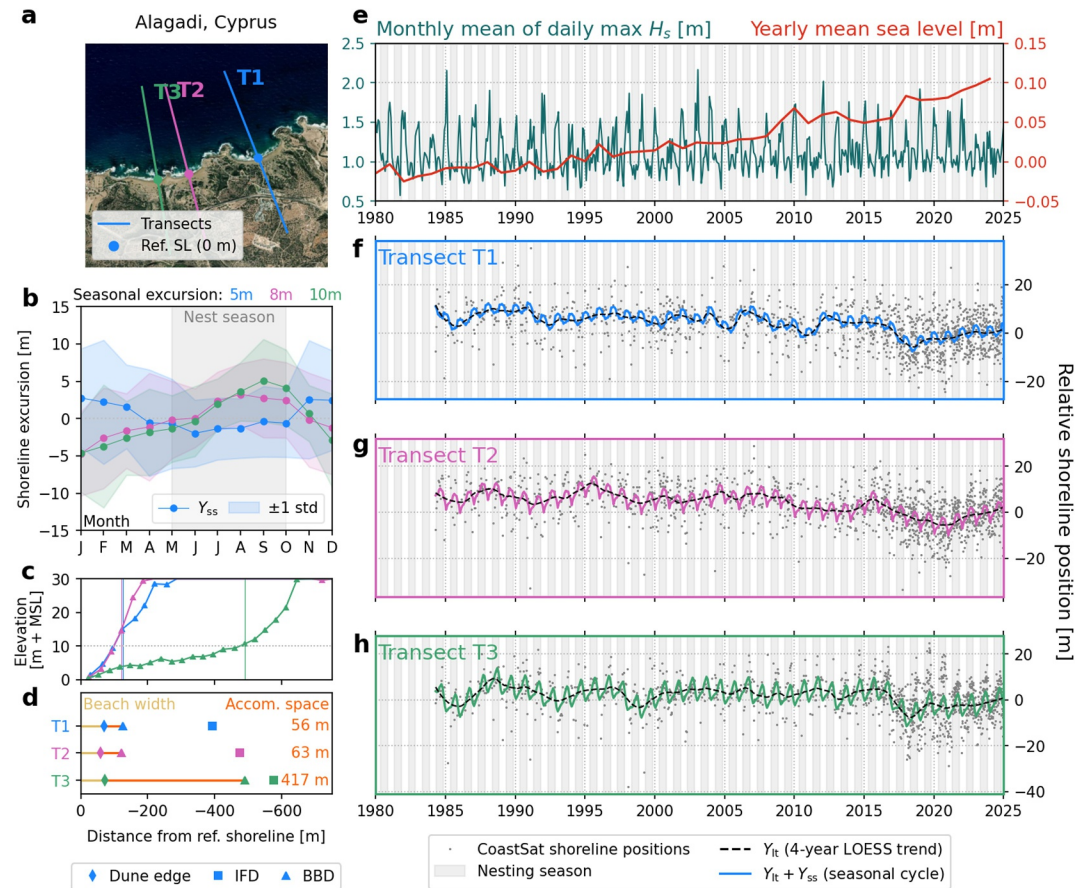


Figure D9. Shoreline and accommodation space analysis for Alagadi, Cyprus: (a) Satellite image showing the transects and reference shoreline position (Ref. SL); (b) Seasonal shoreline component, Y_{ss} , at each transect; (c) Backbeach elevation profiles, with vertical lines denoting the first point above 10 m + MSL; (d) Beach width and accommodation space at each transect; (e) Historical wave and water level time series; (f, g) Observed and decomposed (long-term and seasonal) shoreline position time series at each transect.

Figure D10

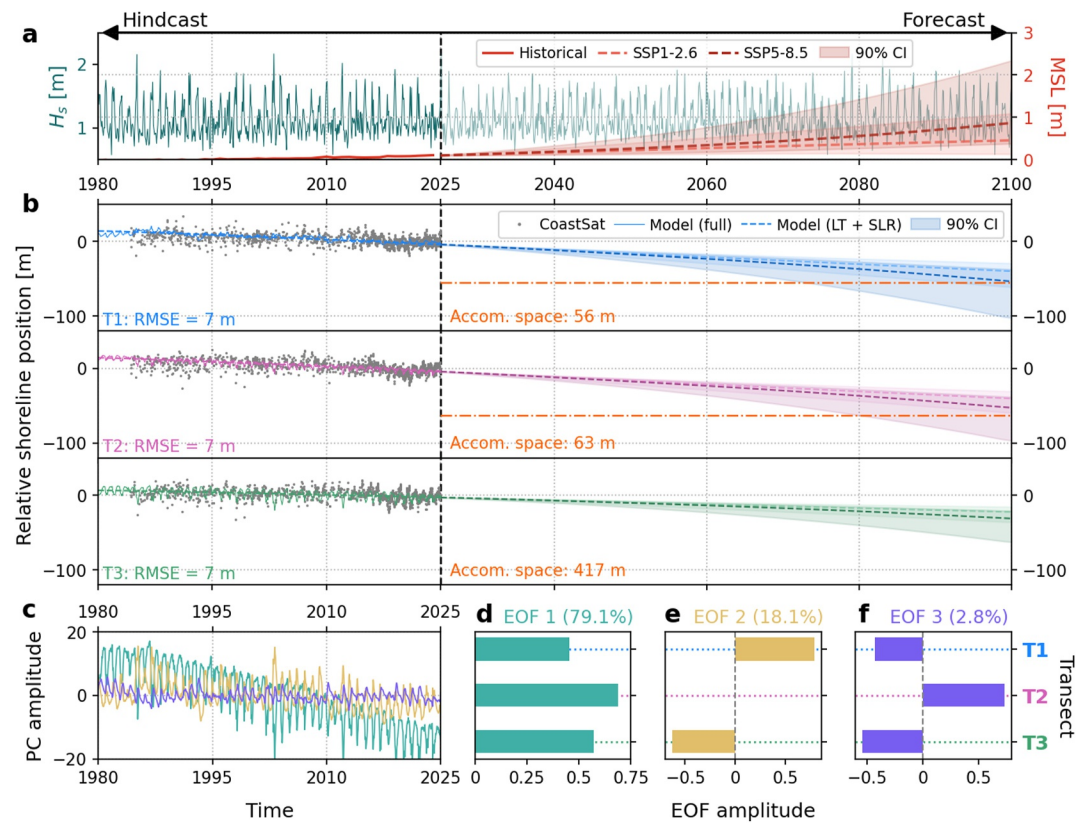


Figure D10. Shoreline modeling results at Alagadi, Cyprus. (a) Wave and sea level time series used to force the model; (b) Modeled shoreline position at each transect for the hindcast (1980–2025) and forecast (2025–2100) periods. Gray dots are the CoastSat shorelines, solid lines represent the full model results, and dashed lines only include the long-term trend (v_{lt}) and sea level rise (SLR) components. In the forecasts, the two dashed lines represent the median SSP1–2.6 (lighter color) and SSP5–8.5 (darker color) SLR projections, while the shading indicates the area between the 5th and 95th percentile; (c) Amplitude of the three PCs over the hindcast period; (d–f) Amplitudes of the three EOFs at each transect and percentage of explained variance.

Figure D11

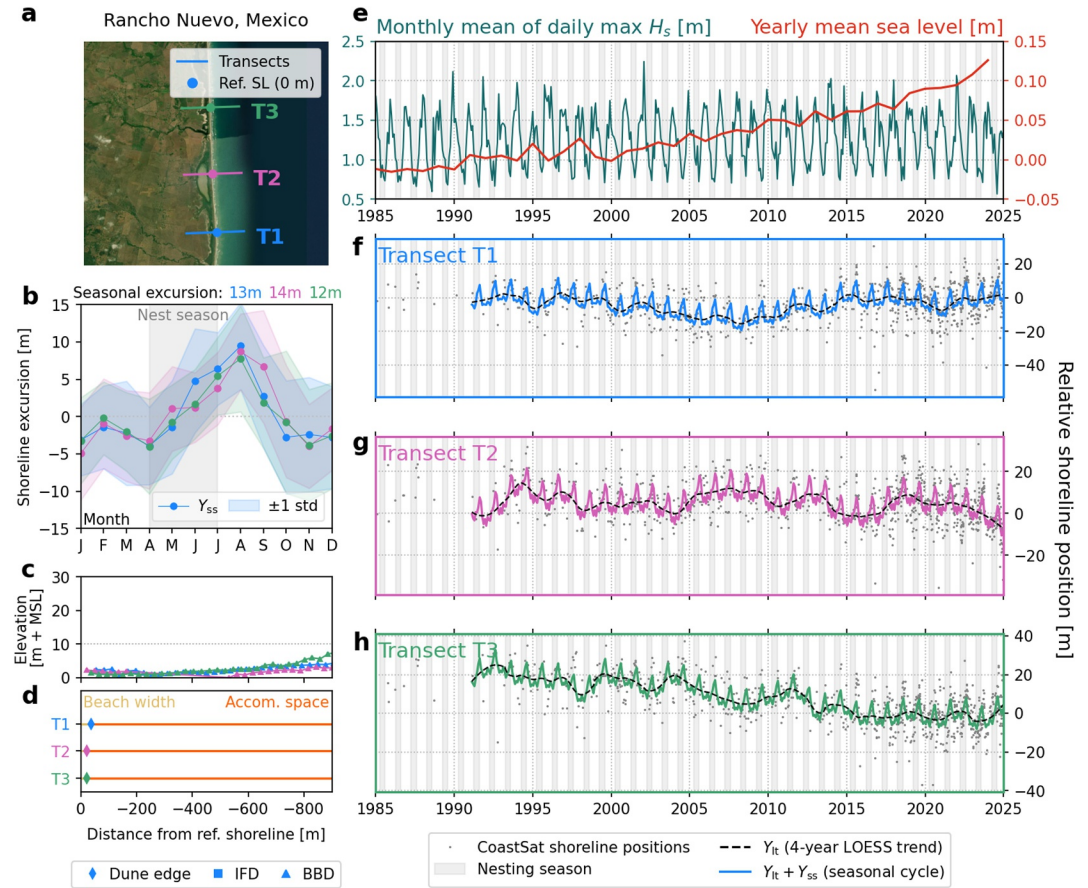


Figure D11. Shoreline and accommodation space analysis for Rancho Nuevo, Mexico: (a) Satellite image showing the transects and reference shoreline position (Ref. SL); (b) Seasonal shoreline component, Y_{ss} , at each transect; (c) Backbeach elevation profiles, with vertical lines denoting the first point above 10 m + MSL; (d) Beach width and accommodation space at each transect; (e) Historical wave and water level time series; (f, g) Observed and decomposed (long-term and seasonal) shoreline position time series at each transect.

Figure D12

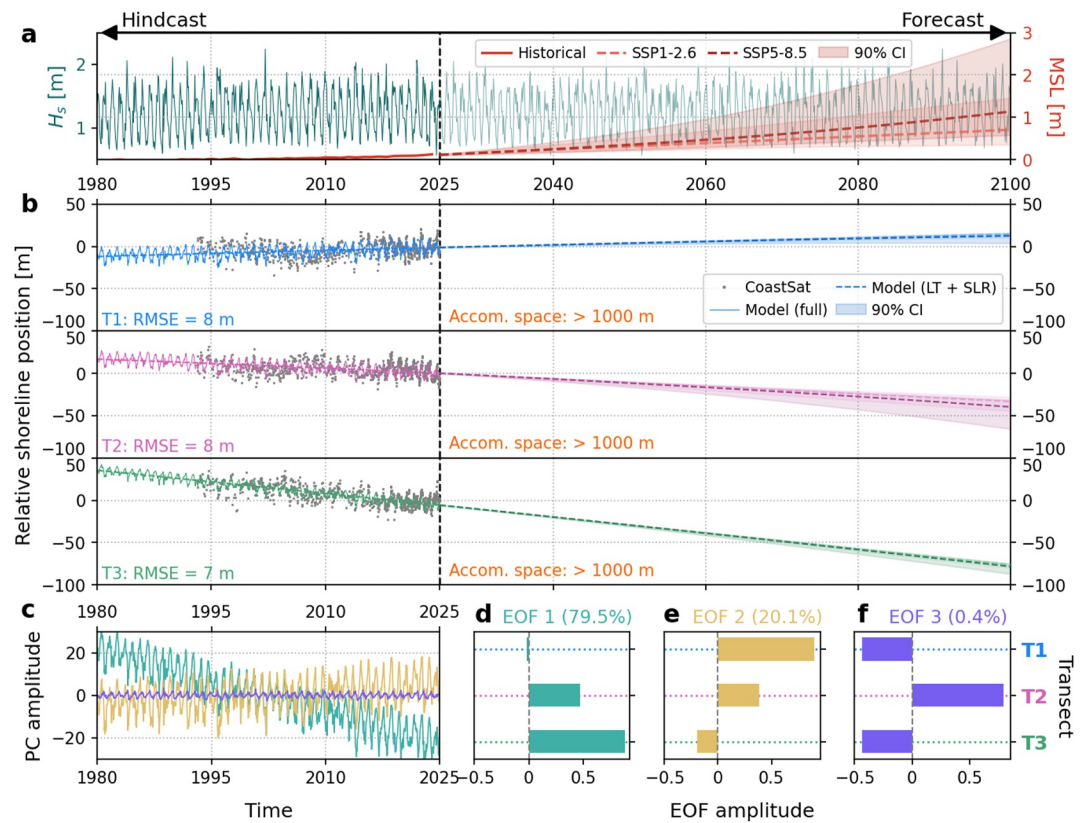


Figure D12. Shoreline modeling results at Rancho Nuevo, Mexico. (a) Wave and sea level time series used to force the model; (b) Modeled shoreline position at each transect for the hindcast (1980–2025) and forecast (2025–2100) periods. Gray dots are the CoastSat shorelines, solid lines represent the full model results, and dashed lines only include the long-term trend (v_{lt}) and sea level rise (SLR) components. In the forecasts, the two dashed lines represent the median SSP1–2.6 (lighter color) and SSP5–8.5 (darker color) SLR projections, while the shading indicates the area between the 5th and 95th percentile; (c) Amplitude of the three PCs over the hindcast period; (d–f) Amplitudes of the three EOFs at each transect and percentage of explained variance.

Figure D13

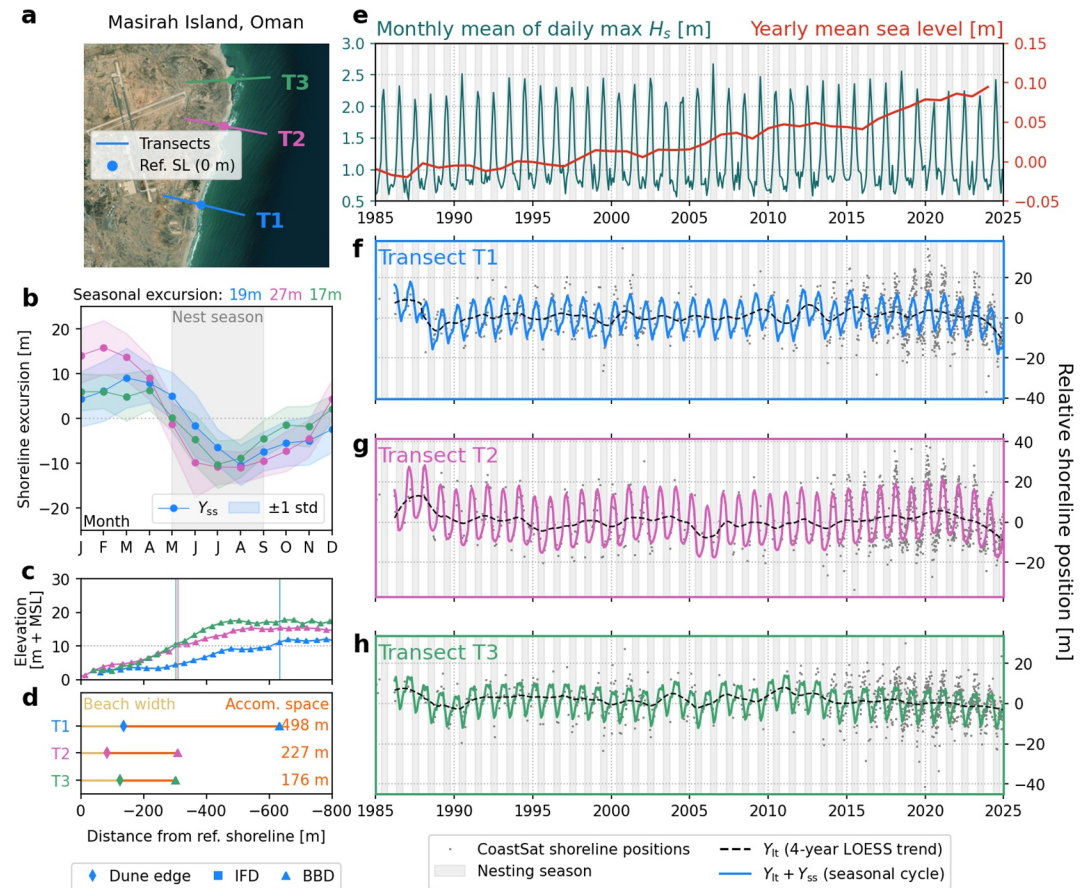


Figure D13. Shoreline and accommodation space analysis for Maşīrah Island, Oman: (a) Satellite image showing the transects and reference shoreline position (Ref. SL); (b) Seasonal shoreline component, Y_{ss} , at each transect; (c) Backbeach elevation profiles, with vertical lines denoting the first point above 10 m + MSL; (d) Beach width and accommodation space at each transect; (e) Historical wave and water level time series; (f, g) Observed and decomposed (long-term and seasonal) shoreline position time series at each transect.

Figure D14

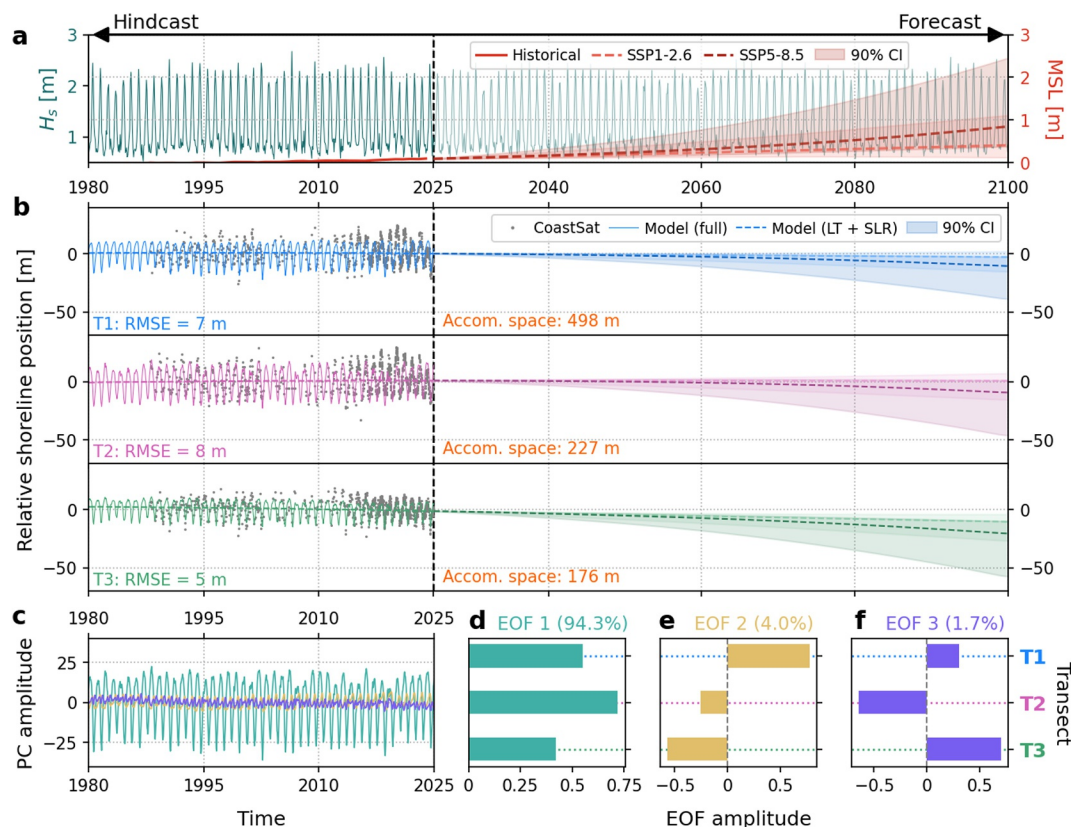


Figure D14. Shoreline modeling results at Maşīrah Island, Oman. (a) Wave and sea level time series used to force the model; (b) Modeled shoreline position at each transect for the hindcast (1980–2025) and forecast (2025–2100) periods. Gray dots are the CoastSat shorelines, solid lines represent the full model results, and dashed lines only include the long-term trend (v_{lt}) and sea level rise (SLR) components. In the forecasts, the two dashed lines represent the median SSP1–2.6 (lighter color) and SSP5–8.5 (darker color) SLR projections, while the shading indicates the area between the 5th and 95th percentile; (c) Amplitude of the three PCs over the hindcast period; (d–f) Amplitudes of the three EOFs at each transect and percentage of explained variance.

Disclaimer

Any use of trade, firm, or product names is for descriptive purposes only and does not imply endorsement by the U.S. Government.

Conflict of Interest

The authors declare no conflicts of interest relevant to this study.

Data Availability Statement

All generated and extracted data underlying the analyses presented in this chapter (including the model code) are publicly available through the 4TU.ResearchData repository via Christiaanse, Vitousek, et al. (2025). All global data sets and tools used in this study are also available online, for access please refer to the following references: Vos, Splinter, et al. (2019) for CoastSat; Pronk et al. (2024) for DeltaDTM; Hersbach et al. (2018) for ERA5; Muis et al. (2020) for GTSM; Garner et al. (2021) for the IPCC AR6 SLR projections; and Calkoen et al. (2025) for GCTS and a guide on extracting building footprints from Overture maps.

Acknowledgments

We would like to acknowledge the following Grant, which provided the digital infrastructure to make computations with the global data sets: EINF-14436 “Coastal Science with AI in a Changing Climate”. Further, we thank Ir. Floris Calkoen for his guidance with using GCTS and Overture Maps, Dr. Kilian Vos for his advice with using CoastSat, and Ir. Étienne Kras for early discussions and work on this project.

References

Abdulsalam, M. B., Jaramillo, C., de Freitas, L., González, M., & Antolínez, J. A. (2025). Assessing shoreline orientation variation across diverse coastal environments. *Coastal Engineering*, 200, 104770. <https://doi.org/10.1016/j.coastaleng.2025.104770>

Ackerman, R. A. (1997). The nest environment and the embryonic development of sea turtles. In P. L. Lutz & J. A. Musick (Eds.), *The biology of sea turtles* (Vol. 1, pp. 83–106). CRC Press.

Anarde, K. A., Moore, L. J., Murray, A. B., & Reeves, I. R. B. (2024). The future of developed barrier systems: 1. Pathways toward uninhabitability, drowning, and rebound. *Earth's Future*, 12(4), e2023EF003672. <https://doi.org/10.1029/2023EF003672>

Antolínez, J. A. A., Méndez, F. J., Anderson, D., Ruggiero, P., & Kaminsky, G. M. (2019). 6). Predicting climate-driven coastlines with a simple and efficient multiscale model. *Journal of Geophysical Research: Earth Surface*, 124(6), 1596–1624. <https://doi.org/10.1029/2018JF004790>

Antolínez, J. A. A., Murray, A. B., Méndez, F. J., Moore, L. J., Farley, G., & Wood, J. (2018). Downscaling changing coastlines in a changing climate: The hybrid approach. *Journal of Geophysical Research: Earth Surface*, 123(2), 229–251. <https://doi.org/10.1002/2017JF004367>

Ashton, A., Murray, A. B., & Arnoult, O. (2001). Formation of coastline features by large-scale instabilities induced by high-angle waves. *Nature*, 414(6861), 296–300. <https://doi.org/10.1038/35104541>

Barbier, E. B., Hacker, S. D., Kennedy, C., Koch, E. W., Stier, A. C., & Silliman, B. R. (2011). The value of estuarine and coastal ecosystem services. *Ecological Monographs*, 81(2), 169–193. <https://doi.org/10.1890/10-1510.1>

Barnard, P. L., Short, A. D., Harley, M. D., Splinter, K. D., Vitousek, S., Turner, I. L., et al. (2015). Coastal vulnerability across the Pacific dominated by El Niño/Southern Oscillation. *Nature Geoscience*, 8(10), 801–807. <https://doi.org/10.1038/ngeo2539>

Beber, I., Sellés-Ríos, B., & Whitworth, A. (2024). Future sea-level rise impacts to Olive Ridley (*Lepidochelys olivacea*) and Green Sea Turtle (*Chelonia mydas*) nesting habitat on the Osa Peninsula, Costa Rica. *Climate Change Ecology*, 7, 100085. <https://doi.org/10.1016/j.ecochg.2024.100085>

Bergsma, E. W., Almar, R., Rolland, A., Binet, R., Brodie, K. L., & Bak, A. S. (2021). Coastal morphology from space: A showcase of monitoring the topography-bathymetry continuum. *Remote Sensing of Environment*, 261, 112469. <https://doi.org/10.1016/j.rse.2021.112469>

Bevan, E., Wibbels, T., Najera, B. M. Z., Martínez, M. A. C., Martínez, L. A. S., Reyes, D. J. L., et al. (2014). In situ nest and hatchling survival at Rancho Nuevo, the primary nesting beach of the Kemp's ridley sea turtle, *Lepidochelys Kempii*. *Herpetological Conservation and Biology*, 9(3), 563–577. Retrieved from https://www.herpconbio.org/Volume_9/Issue_3/Bevan_et_al_2014.pdf

Bjorndal, K. A., Wetherall, J. A., Bolten, A. B., & Mortimer, J. A. (1999). Twenty-Six years of green turtle nesting at tortuguero, Costa Rica: An encouraging trend. *Conservation Biology*, 13(1), 126–134. <https://doi.org/10.1046/j.1523-1739.1999.97329.x>

Bosboom, J., Reniers, A. J. H. M., & Luijendijk, A. P. (2014). 12). On the perception of morphodynamic model skill. *Coastal Engineering*, 94, 112–125. <https://doi.org/10.1016/j.coastaleng.2014.08.008>

Broderick, A. C., Glen, F., Godley, B. J., & Hays, G. C. (2002). Estimating the number of green and loggerhead turtles nesting annually in the Mediterranean. *Oryx*, 36(3), 227–235. <https://doi.org/10.1017/S0030605302000431>

Calkoen, F. R., Luijendijk, A. P., Vos, K., Kras, E., & Baart, F. (2025). Enabling coastal analytics at planetary scale. *Environmental Modelling & Software*, 183, 106257. <https://doi.org/10.1016/j.envsoft.2024.106257>

Cappellari, M., McDermid, R. M., Alatalo, K., Blitz, L., Bois, M., Bournaud, F., et al. (2013). The ATLAS3D project – XX. Mass–size and mass– σ distributions of early-type galaxies: Bulge fraction drives kinematics, mass-to-light ratio, molecular gas fraction and stellar initial mass function. *Monthly Notices of the Royal Astronomical Society*, 432(3), 1862–1893. <https://doi.org/10.1093/mnras/stt644>

Casale, P., & Tucker, A. D. (2017). *Caretta caretta* (amended version of 2015 assessment). <https://doi.org/10.2305/IUCN.UK.2017-2.RLTS.T3897A119333622.en>

Cassill, D. L. (2021). 1). Multiple maternal risk-management adaptations in the loggerhead sea turtle (*Caretta caretta*) mitigate clutch failure caused by catastrophic storms and predators. *Scientific Reports*, 11(1), 2491. <https://doi.org/10.1038/s41598-021-81968-0>

Castelle, B., Marieu, V., Bujan, S., Splinter, K. D., Robinet, A., Sénéchal, N., & Ferreira, S. (2015). Impact of the winter 2013–2014 series of severe Western Europe storms on a double-barred sandy coast: Beach and dune erosion and megacusp embayments. *Geomorphology*, 238, 135–148. <https://doi.org/10.1016/j.geomorph.2015.03.006>

Castelle, B., Masselink, G., Scott, T., Stokes, C., Konstantinou, A., Marieu, V., & Bujan, S. (2021). Satellite-derived shoreline detection at a high-energy meso-macrotidal beach. *Geomorphology*, 383, 107707. <https://doi.org/10.1016/j.geomorph.2021.107707>

Castelle, B., Ritz, A., Marieu, V., Nicolae Lerma, A., & Vandenhove, M. (2022). Primary drivers of multidecadal spatial and temporal patterns of shoreline change derived from optical satellite imagery. *Geomorphology*, 413, 108360. <https://doi.org/10.1016/j.geomorph.2022.108360>

Christiaanse, J. C., Antolínez, J. A. A., Luijendijk, A. P., Athanasiou, P., Duarte, C. M., & Aarninkhof, S. (2024). Distribution of global sea turtle nesting explained from regional-scale coastal characteristics. *Scientific Reports*, 14, 752. <https://doi.org/10.1038/s41598-023-50239-5>

Christiaanse, J. C., Reniers, A. J. H. M., Aarninkhof, S. G. J., Ostertag, E. F., Nel, R., Duarte, C. M., & Antolínez, J. A. A. (2025). Aiding sea turtle conservation through coastal management. *Frontiers in Marine Science*, 12, 1669885. <https://doi.org/10.3389/fmars.2025.1669885>

Christiaanse, J. C., Vitousek, S., Reniers, A. J. H. M., & Antolínez, J. A. A. (2025). Data underlying the publication “Vulnerability of Key Sea Turtle Nesting Beaches to Future Erosion and Sea Level Rise” [Dataset]. 4TU. ResearchData. <https://doi.org/10.4121/0a7cf460-e3da-4f80-aa20-f41eb7f9ef93>

Christianen, M. J. A., Smulders, F. O. H., Vonk, J. A., Becking, L. E., Bouma, T. J., Engel, S. M., et al. (2023). Seagrass ecosystem multifunctionality under the rise of a flagship marine megaherbivore. *Global Change Biology*, 29(1), 215–230. <https://doi.org/10.1111/gcb.16464>

Cleveland, R. B., Cleveland, W. S., McRae, J. E., & Terpenning, I. (1990). STL: A seasonal-trend decomposition procedure based on loess. *Journal of Official Statistics*, 6(1), 3–73.

Cleveland, W. S. (1979). Robust locally weighted regression and smoothing scatterplots. *Journal of the American Statistical Association*, 74(368), 829–836. <https://doi.org/10.1080/01621459.1979.10481038>

CNES. (2024). FES2022 (finite element solution) ocean tide (Version 2022) [Dataset]. <https://doi.org/10.24400/527896/A01-2024.004>

Cooper, J. A. G., Masselink, G., Coco, G., Short, A. D., Castelle, B., Rogers, K., et al. (2020). Sandy beaches can survive sea-level rise. *Nature Climate Change*, 10(11), 993–995. <https://doi.org/10.1038/s41558-020-00934-2>

Cutler, M. V. W., Vos, K., Branson, P., Hansen, J. E., O’Leary, M., Browne, N. K., & Lowe, R. J. (2020). Interannual response of Reef Islands to climate-driven variations in water level and wave climate. *Remote Sensing*, 12(24), 4089. <https://doi.org/10.3390/rs12244089>

Davidson, M., Lewis, R., & Turner, I. (2010). Forecasting seasonal to multi-year shoreline change. *Coastal Engineering*, 57(6), 620–629. <https://doi.org/10.1016/j.coastaleng.2010.02.001>

Defeo, O., McLachlan, A., Schoeman, D. S., Schlacher, T. A., Dugan, J., Jones, A., et al. (2009). Threats to sandy beach ecosystems: A review. *Estuarine, Coastal and Shelf Science*, 81(1), 1–12. <https://doi.org/10.1016/j.ecss.2008.09.022>

- Dong, Z., Elko, N., Robertson, Q., & Rosati, J. (2018). Quantifying beach and dune resilience using the coastal resilience index. *Coastal Engineering Proceedings*, 1(36), 30. <https://doi.org/10.9753/icce.v36.papers.30>
- Duarte, C. M., Agusti, S., Barbier, E., Britten, G. L., Castilla, J. C., Gattuso, J.-P., et al. (2020). Rebuilding marine life. *Nature*, 580(7801), 39–51. <https://doi.org/10.1038/s41586-020-2146-7>
- Duveiller, G., Fasbender, D., & Meroni, M. (2016). Revisiting the concept of a symmetric index of agreement for continuous datasets. *Scientific Reports*, 6(1), 19401. <https://doi.org/10.1038/srep19401>
- Erikson, L. H., O'Neill, A. C., Barnard, P. L., Vitousek, S., & Limber, P. W. (2017). Climate change-driven cliff and beach evolution at decadal to centennial time scales. In T. Aagaard, R. Deigaard, & D. Fuhrman (Eds.), *Proceedings of coastal dynamics 2017* (pp. 125–136). Helsingor, DK. Esri. (2024). World imagery basemap. Retrieved from https://services.arcgis.com/ArcGIS/rest/services/World_Imagery/MapServer
- Fish, M. R., Côte, I. M., Gill, J. A., Jones, A. P., Renshoff, S., & Watkinson, A. R. (2005). Predicting the impact of sea-level rise on Caribbean Sea turtle nesting habitat. *Conservation Biology*, 19(2), 482–491. <https://doi.org/10.1111/j.1523-1739.2005.00146.x>
- Fossette, S., Kelle, L., Girondot, M., Goverse, E., Hilterman, M. L., Verhage, B., et al. (2008). The world's largest leatherback rookeries: A review of conservation-oriented research in French Guiana/Suriname and Gabon. *Journal of Experimental Marine Biology and Ecology*, 356(1–2), 69–82. <https://doi.org/10.1016/j.jembe.2007.12.024>
- Fox-Kemper, B., Hewitt, H. T., Xiao, C., Adalgeirsdóttir, G., Drijfhout, S. S., Edwards, T. L., et al. (Eds.). (2021). *Climate change 2021 – The physical science basis* (pp. 1211–1362). Cambridge University Press. <https://doi.org/10.1017/9781009157896.011>
- French, J., Payo, A., Murray, B., Orford, J., Eliot, M., & Cowell, P. (2016). Appropriate complexity for the prediction of coastal and estuarine geomorphic behaviour at decadal to centennial scales. *Geomorphology*, 256, 3–16. <https://doi.org/10.1016/j.geomorph.2015.10.005>
- Fuentes, M. M. P. B., Limpus, C. J., Hamann, M., & Dawson, J. (2010). Potential impacts of projected sea-level rise on sea turtle rookeries. *Aquatic Conservation: Marine and Freshwater Ecosystems*, 20(2), 132–139. <https://doi.org/10.1002/aqc.1088>
- Garcia, D. (2010). Robust smoothing of gridded data in one and higher dimensions with missing values. *Computational Statistics & Data Analysis*, 54(4), 1167–1178. <https://doi.org/10.1016/j.csda.2009.09.020>
- Garcin, M., Vende-Leclerc, M., Read, T., Oremus, M., & Bourgoigne, H. (2022). Assessment method of the sea turtle-nesting habitat of small reef islands. *Journal of Coastal Conservation*, 26(3), 24. <https://doi.org/10.1007/s11852-022-00870-7>
- Garner, G. G., Hermans, T., Kopp, R. E., Slangen, A. B. A., Edwards, T. L., Levermann, A., et al. (2021). IPCC AR6 Sea Level projections. Version 20210809 [Dataset]. <https://doi.org/10.5281/zenodo.5914709>
- Godley, B. J., Broderick, A. C., & Hays, G. C. (2001). Nesting of green turtles (*Chelonia mydas*) at Ascension Island, South Atlantic. *Biological Conservation*, 97(2), 151–158. [https://doi.org/10.1016/S0006-3207\(00\)00107-5](https://doi.org/10.1016/S0006-3207(00)00107-5)
- Gomez-de la Peña, E., Coco, G., Whittaker, C., & Montañó, J. (2023). On the use of convolutional deep learning to predict shoreline change. *Earth Surface Dynamics*, 11(6), 1145–1160. <https://doi.org/10.5194/esurf-11-1145-2023>
- Gorelick, N., Hancher, M., Dixon, M., Ilyushchenko, S., Thau, D., & Moore, R. (2017). Google Earth Engine: Planetary-scale geospatial analysis for everyone. *Remote Sensing of Environment*, 202, 18–27. <https://doi.org/10.1016/j.rse.2017.06.031>
- Harley, M. D., Turner, I. L., & Short, A. D. (2015). New insights into embayed beach rotation: The importance of wave exposure and cross-shore processes. *Journal of Geophysical Research: Earth Surface*, 120(8), 1470–1484. <https://doi.org/10.1002/2014JF003390>
- Hawkes, L., Broderick, A., Godfrey, M., & Godley, B. (2009). Climate change and marine turtles. *Endangered Species Research*, 7(2), 137–154. <https://doi.org/10.3354/esr00198>
- Hersbach, H., Bell, B., Berrisford, P., Biavati, G., Horányi, A., Muñoz Sabater, J., et al. (2018). ERA5 hourly data on single levels from 1979 to present [Dataset]. <https://doi.org/10.24381/cds.adbb2d47>
- Holthuijsen, L. H. (2007). *Waves in Oceanic and coastal waters*. Cambridge University Press. <https://doi.org/10.1017/CBO9780511618536>
- Hunt, E., Davidson, M., Steele, E. C. C., Amies, J. D., Scott, T., & Russell, P. (2023). Shoreline modelling on timescales of days to decades. *Cambridge Prisms: Coastal Futures*, 1, e16. <https://doi.org/10.1017/CFT.2023.5>
- Khojasteh, D., Glamore, W., Heimhuber, V., & Felder, S. (2021). Sea level rise impacts on estuarine dynamics: A review. *Science of The Total Environment*, 780, 146470. <https://doi.org/10.1016/j.scitotenv.2021.146470>
- Kopp, R. E., Garner, G. G., Hermans, T. H. J., Jha, S., Kumar, P., Reedy, A., et al. (2023). The framework for assessing changes to Sea-level (FACTS) v1.0: A platform for characterizing parametric and structural uncertainty in future global, relative, and extreme sea-level change. *Geoscientific Model Development*, 16(24), 7461–7489. <https://doi.org/10.5194/gmd-16-7461-2023>
- Kroon, A., Christiaan, J. C., Luijendijk, A. P., Schipper, M. A. d., & Ranasinghe, R. (2025). Parameter uncertainty in medium-term coastal morphodynamic modeling. *Scientific Reports*, 15(1), 18471. <https://doi.org/10.1038/s41598-025-02300-8>
- Laloë, J.-O., & Hays, G. C. (2023). Can a present-day thermal niche be preserved in a warming climate by a shift in phenology? A case study with sea turtles. *Royal Society Open Science*, 10(2), 221002. <https://doi.org/10.1098/rsos.221002>
- Lansu, E. M., Reijers, V. C., Höfer, S., Luijendijk, A., Rietkerk, M., Wassen, M. J., et al. (2024). A global analysis of how human infrastructure squeezes sandy coasts. *Nature Communications*, 15(1), 432. <https://doi.org/10.1038/s41467-023-44659-0>
- Leaman, C. K., Harley, M. D., Splinter, K. D., Thrane, M. C., Kinsela, M. A., & Turner, I. L. (2021). A storm hazard matrix combining coastal flooding and beach erosion. *Coastal Engineering*, 170, 104001. <https://doi.org/10.1016/j.coastaleng.2021.104001>
- Le Cozannet, G., Bulteau, T., Castelle, B., Ranasinghe, R., Wöppelmann, G., Rohmer, J., et al. (2019). Quantifying uncertainties of sandy shoreline change projections as sea level rises. *Scientific Reports*, 9, 42. <https://doi.org/10.1038/s41598-018-37017-4>
- López-Dóriga, U., & Jiménez, J. A. (2020). Impact of relative sea-level rise on low-lying coastal areas of Catalonia, NW mediterranean, Spain. *Water*, 12(11), 3252. <https://doi.org/10.3390/w12113252>
- Luijendijk, A., Hagenaars, G., Ranasinghe, R., Baart, F., Donchyts, G., & Aarninkhof, S. (2018). The State of the world's beaches. *Scientific Reports*, 8(1), 6641. <https://doi.org/10.1038/s41598-018-24630-6>
- Mao, Y., Coco, G., Vitousek, S., Antolinez, J. A. A., Azorakos, G., Banno, M., et al. (2025). Benchmarking shoreline prediction models over multi-decadal timescales. *Communications Earth & Environment*, 6(1), 581. <https://doi.org/10.1038/s43247-025-02550-4>
- Marco, A., Abella, E., Liria-Loza, A., Martins, S., López, O., Jiménez-Bordón, S., et al. (2012). Abundance and exploitation of loggerhead turtles nesting in Boa Vista island, Cape Verde: The only substantial rookery in the eastern Atlantic. *Animal Conservation*, 15(4), 351–360. <https://doi.org/10.1111/j.1469-1795.2012.00547.x>
- Marcovaldi, M. A., Lopez, G. G., Soares, L. S., Santos, A. J., Bellini, C., & Barata, P. C. (2007). Fifteen years of Hawksbill Sea Turtle (*Eretmochelys imbricata*) nesting in Northern Brazil. *Chelonian Conservation and Biology*, 6(2), 223–228. [https://doi.org/10.2744/1071-8443\(2007\)6\[223:FYOHST\]2.0.CO;2](https://doi.org/10.2744/1071-8443(2007)6[223:FYOHST]2.0.CO;2)
- Marcovaldi, M. A., Vieitas, C. F., & Godfrey, M. H. (1999). Nesting and conservation management of hawksbill turtles (*Eretmochelys imbricata*) in Northern Bahia, Brazil. In *Chelonian Conservation and Biology* (Vol. 3, pp. 301–307).

- Martins, S., Patrício, R., Clarke, L. J., de Santos Loureiro, N., & Marco, A. (2022). High variability in nest site selection in a loggerhead turtle rookery. In B. Vista Island & C. Verde (Eds.) *Journal of Experimental Marine Biology and Ecology* (Vol. 556, p. 151798). <https://doi.org/10.1016/J.JEMBE.2022.151798>
- Masselink, G., Beetham, E., & Kench, P. (2020). Coral reef islands can accrete vertically in response to sea level rise. *Science Advances*, 6(24), 3656–3666. <https://doi.org/10.1126/sciadv.aay3656>
- Mast, R. B., Hutchinson, B. J., Villegas, P. E., & Bandimere, A. (2025). SWOT report volume 20 (Tech. Rep.). SWOT: The state of the world's sea turtles. Retrieved from <https://www.seaturtlestatus.org/swot-report-vol-20>
- Mazaris, A. D., Almpandou, V., Wallace, B. P., Pantis, J. D., & Schofield, G. (2014). A global gap analysis of sea turtle protection coverage. *Biological Conservation*, 173, 17–23. <https://doi.org/10.1016/j.biocon.2014.03.005>
- McClenachan, L., Jackson, J. B., & Newman, M. J. (2006). Conservation implications of historic sea turtle nesting beach loss. *Frontiers in Ecology and the Environment*, 4(6), 290–296. [https://doi.org/10.1890/1540-9295\(2006\)4\[290:CIOHST\]2.0.CO;2](https://doi.org/10.1890/1540-9295(2006)4[290:CIOHST]2.0.CO;2)
- Meylan, A. (1988). Spongivory in hawksbill turtles: A diet of glass. *Science*, 239(4838), 393–395. <https://doi.org/10.1126/science.239.4838.393>
- Miller, J. K., & Dean, R. G. (2007a). Shoreline variability via empirical orthogonal function analysis: Part II relationship to nearshore conditions. *Coastal Engineering*, 54(2), 133–150. <https://doi.org/10.1016/j.coastaleng.2006.08.014>
- Miller, J. K., & Dean, R. G. (2007b). Shoreline variability via empirical orthogonal function analysis: Part I temporal and spatial characteristics. *Coastal Engineering*, 54(2), 111–131. <https://doi.org/10.1016/j.coastaleng.2006.08.013>
- Montaño, J., Coco, G., Antolínez, J. A. A., Beuzen, T., Bryan, K. R., Cagigal, L., et al. (2020). Blind testing of shoreline evolution models. *Scientific Reports*, 10(1), 2137. <https://doi.org/10.1038/s41598-020-59018-y>
- Moore, L. J., Hacker, S. D., Breithaupt, J., de Vries, S., Miller, T., Ruggiero, P., & Zinnert, J. C. (2025). Ecomorphodynamics of coastal foredune evolution. *Nature Reviews Earth & Environment*, 6(6), 417–432. <https://doi.org/10.1038/s43017-025-00672-z>
- Moore, L. J., & Murray, A. B. (2022). Islands on the move. *Nature Geoscience*, 15(8), 602–603. <https://doi.org/10.1038/s41561-022-01000-6>
- Morim, J., Hemer, M., Wang, X. L., Cartwright, N., Trenham, C., Semedo, A., et al. (2019). 9. Robustness and uncertainties in global multivariate wind-wave climate projections. *Nature Climate Change*, 9(9), 711–718. <https://doi.org/10.1038/s41558-019-0542-5>
- Morim, J., Trenham, C., Hemer, M., Wang, X. L., Mori, N., Casas-Prat, M., et al. (2020). A global ensemble of ocean wave climate projections from CMIP5-driven models. *Scientific Data*, 7(1), 105. <https://doi.org/10.1038/s41597-020-0446-2>
- Morim, J., Wahl, T., Rasmussen, D. J., Calafat, F. M., Vitousek, S., Dangendorf, S., et al. (2025). Observations reveal changing coastal storm extremes around the United States. *Nature Climate Change*, 15(5), 538–545. <https://doi.org/10.1038/s41558-025-02315-z>
- Mortimer, J. A. (1995). Teaching critical concepts for the conservation of sea turtles. *Marine Turtle Newsletter*, 71(4). Retrieved from <http://seaturtle.org/mtn/archives/mtn71/mtn71p1.shtml>
- Muis, S., Irazoqui Apecechea, M., Dullaart, J., de Lima Rego, J., Madsen, K. S., Su, J., et al. (2020). A high-resolution global dataset of extreme sea levels, tides, and storm surges, including future projections. *Frontiers in Marine Science*, 7, 512955. <https://doi.org/10.3389/fmars.2020.00263>
- Murray, A. B., Coco, G., & Goldstein, E. B. (2014). 6. Cause and effect in geomorphic systems: Complex systems perspectives. *Geomorphology*, 214, 1–9. <https://doi.org/10.1016/j.geomorph.2014.03.001>
- Nel, R., Campbell, E. E., Harris, L., Hauser, L., Schoeman, D. S., McLachlan, A., et al. (2014). The status of sandy beach science: Past trends, progress, and possible futures. *Estuarine, Coastal and Shelf Science*, 150(PA), 1–10. <https://doi.org/10.1016/j.ecss.2014.07.016>
- Ocana, M., Harfush-Melendez, M., & Heppell, S. S. (2012). Mass nesting of olive ridley sea turtles *Lepidochelys olivacea* at La Escobilla, Mexico: Linking nest density and rates of destruction. *Endangered Species Research*, 16(1), 45–54. <https://doi.org/10.3354/ESR00388>
- Passeri, D. L., Hagen, S. C., Medeiros, S. C., Bilskie, M. V., Alizad, K., & Wang, D. (2015). The dynamic effects of sea level rise on low-gradient coastal landscapes: A review. *Earth's Future*, 3(6), 159–181. <https://doi.org/10.1002/2015EF000298doi:10.1002/2015EF000298>
- Patrício, A. R., Hawkes, L. A., Monsinjon, J. R., Godley, B. J., & Fuentes, M. M. P. B. (2021). Climate change and marine turtles: Recent advances and future directions. *Endangered Species Research*, 44, 363–395. <https://doi.org/10.3354/esr01110>
- Pianca, C., Holman, R., & Siegle, E. (2015). 3. Shoreline variability from days to decades: Results of long-term video imaging. *Journal of Geophysical Research: Oceans*, 120(3), 2159–2178. <https://doi.org/10.1002/2014JC010329>
- Pike, D. A., & Stiner, J. C. (2007). Sea turtle species vary in their susceptibility to tropical cyclones. *Oecologia*, 153(2), 471–478. <https://doi.org/10.1007/s00442-007-0732-0>
- Pontee, N. (2013). Defining coastal squeeze: A discussion. *Ocean & Coastal Management*, 84, 204–207. <https://doi.org/10.1016/j.ocecoaman.2013.07.010>
- Prince, R. I. T. (1994). Shark Bay world heritage area: An important loggerhead nesting site. *Marine Turtle Newsletter*, 67, 5–6. Retrieved from <http://www.seaturtle.org/mtn/archives/mtn67/mtn67p5.shtml>
- Pronk, M., Hooijer, A., Eilander, D., Haag, A., de Jong, T., Voudoukas, M., et al. (2024). 3. DeltaDTM: A global coastal digital terrain model. *Scientific Data*, 11(1), 273. <https://doi.org/10.1038/s41597-024-03091-9>
- Reguero, B. G., Losada, I. J., & Méndez, F. J. (2019). A recent increase in global wave power as a consequence of oceanic warming. *Nature Communications*, 10(1), 205. <https://doi.org/10.1038/s41467-018-08066-0>
- Reinhold, L., & Whiting, A. (2014). High-density loggerhead sea turtle nesting on Dirk Hartog island, Western Australia. *Marine Turtle Newsletter*, 141, 7–10. Retrieved from <http://www.seaturtle.org/mtn/archives/mtn141/mtn141-3.shtml>
- Repina, O., Carvalho, R. C., Coco, G., Antolínez, J. A., de Santiago, I., Harley, M. D., et al. (2025). Evaluating five shoreline change models against 40 years of field survey data at an embayed sandy beach. *Coastal Engineering*, 199, 104738. <https://doi.org/10.1016/j.coastaleng.2025.104738>
- Restrepo, J., Webster, E., Ramos, I., & Valverde, R. (2023). Recent decline of green turtle *Chelonia mydas* nesting trend at Tortuguero, Costa Rica. *Endangered Species Research*, 51, 59–72. <https://doi.org/10.3354/esr01237>
- Rivas, M. L., Rodríguez-Caballero, E., Esteban, N., Carpio, A. J., Barrera-Vilarmau, B., Fuentes, M. M. P. B., et al. (2023). 4. Uncertain future for global sea turtle populations in face of sea level rise. *Scientific Reports*, 13(1), 5277. <https://doi.org/10.1038/s41598-023-31467-1>
- Rogers, K., Saintilan, N., & Copeland, C. (2012). Modelling wetland surface elevation dynamics and its application to forecasting the effects of sea-level rise on estuarine wetlands. *Ecological Modelling*, 244, 148–157. <https://doi.org/10.1016/j.ecolmodel.2012.06.014>
- Rosati, J., Dean, R., & Walton, T. (2013). The modified Bruun Rule extended for landward transport. *Marine Geology*, 340, 71–81. <https://doi.org/10.1016/j.margeo.2013.04.018>
- Shanker, K., Pandav, B., & Choudhury, B. (2004). An assessment of the olive ridley turtle (*Lepidochelys olivacea*) nesting population in Orissa, India. *Biological Conservation*, 115(1), 149–160. [https://doi.org/10.1016/S0006-3207\(03\)00104-6](https://doi.org/10.1016/S0006-3207(03)00104-6)
- Shaver, D. J., & Caillouet Jr, C. W. (2015). Reintroduction of Kemp's ridley (*Lepidochelys kempii*) sea turtle to Padre Island National Seashore, Texas and its connection to head-starting. *Herpetological Conservation and Biology*, 10(1), 378–435. https://www.herpconbio.org/Volume_10/Symposium/Caillouet_et_al_2015.pdf

- Smithers, S. G., & Dawson, J. L. (2023). 1). Beach reprofiling to improve reproductive output at the world's largest remaining green turtle rookery: Raine Island, northern Great Barrier Reef. *Ocean & Coastal Management*, 231, 106385. <https://doi.org/10.1016/j.ocecoaman.2022.106385>
- Sobel, A. H., Camargo, S. J., Hall, T. M., Lee, C.-Y., Tippet, M. K., & Wing, A. A. (2016). Human influence on tropical cyclone intensity. *Science*, 353(6296), 242–246. <https://doi.org/10.1126/science.aaf6574>
- Splinter, K. D., & Coco, G. (2021). Challenges and opportunities in coastal shoreline prediction. *Frontiers in Marine Science*, 8, 788657. <https://doi.org/10.3389/fmars.2021.788657>
- Staines, M. N., Booth, D. T., Laloë, J.-O., & Hays, G. C. (2025). The impact of sea level rise on nesting sea turtles: A global meta-analysis to highlight current understanding and knowledge gaps. *Marine Biology*, 172(11), 171. <https://doi.org/10.1007/s00227-025-04726-0>
- Stokes, H. J., Esteban, N., & Hays, G. C. (2024). Nest site selection in sea turtles shows consistencies across the globe in the face of climate change. *Animal Behaviour*, 208, 59–68. <https://doi.org/10.1016/j.anbehav.2023.12.001>
- Taylor, K. E. (2001). Summarizing multiple aspects of model performance in a single diagram. *Journal of Geophysical Research*, 106(D7), 7183–7192. <https://doi.org/10.1029/2000jd900719>
- Thomas, J. A., Barnard, P. L., Vitousek, S., Erikson, L. H., Parker, K., Nederhoff, K., et al. (2024). The projected exposure and response of a natural barrier island system to climate-driven coastal hazards. *Scientific Reports*, 14(1), 25814. <https://doi.org/10.1038/s41598-024-76749-4>
- Varela, M. R., Patrício, A. R., Anderson, K., Broderick, A. C., DeBell, L., Hawkes, L. A., et al. (2019). Assessing climate change associated sea-level rise impacts on sea turtle nesting beaches using drones, photogrammetry and a novel GPS system. *Global Change Biology*, 25(2), 753–762. <https://doi.org/10.1111/gcb.14526>
- Vitousek, S., Barnard, P. L., & Limber, P. (2017). Can beaches survive climate change? *Journal of Geophysical Research: Earth Surface*, 122(4), 1060–1067. <https://doi.org/10.1002/2017JF004308>
- Vitousek, S., Barnard, P. L., Limber, P., Erikson, L., & Cole, B. (2017). A model integrating longshore and cross-shore processes for predicting long-term shoreline response to climate change. *Journal of Geophysical Research: Earth Surface*, 122(4), 782–806. <https://doi.org/10.1002/2016JF004065>
- Vitousek, S., Buscombe, D., Gomez-de la Peña, E., Calcraft, K., Lundine, M., Splinter, K. D., et al. (2025). Are equilibrium shoreline models just convolutions? *Journal of Geophysical Research: Earth Surface*, 130(6), e2025JF008452. <https://doi.org/10.1029/2025JF008452>
- Vitousek, S., Buscombe, D., Vos, K., Barnard, P. L., Ritchie, A. C., & Warrick, J. A. (2023). The future of coastal monitoring through satellite remote sensing. *Cambridge Prisms: Coastal Futures*, 1, e10. <https://doi.org/10.1017/cft.2022.4>
- Vitousek, S., Cagigal, L., Montaña, J., Rueda, A., Mendez, F., Coco, G., & Barnard, P. L. (2021). The application of ensemble wave forcing to quantify uncertainty of shoreline change predictions. *Journal of Geophysical Research: Earth Surface*, 126(7), e2019JF005506. <https://doi.org/10.1029/2019JF005506>
- Vitousek, S., Vos, K., Splinter, K. D., Erikson, L., & Barnard, P. L. (2023). A model integrating satellite-derived shoreline observations for predicting fine-scale shoreline response to waves and sea-level rise across large coastal regions. *Journal of Geophysical Research: Earth Surface*, 128(7), e2022JF006936. <https://doi.org/10.1029/2022JF006936>
- Vitousek, S., Vos, K., Splinter, K. D., Parker, K., O'Neill, A., Foxgrover, A. C., et al. (2024). Scalable, data-assimilated models predict large-scale shoreline response to waves and sea-level rise. *Scientific Reports*, 14(1), 28029. <https://doi.org/10.1038/s41598-024-77030-4>
- Vos, K., Harley, M. D., Splinter, K. D., Simmons, J. A., & Turner, I. L. (2019). Sub-annual to multi-decadal shoreline variability from publicly available satellite imagery. *Coastal Engineering*, 150, 160–174. <https://doi.org/10.1016/j.coastaleng.2019.04.004>
- Vos, K., Harley, M. D., Splinter, K. D., Walker, A., & Turner, I. L. (2020). 7). Beach slopes from satellite-derived shorelines. *Geophysical Research Letters*, 47(14), e2020GL088365. <https://doi.org/10.1029/2020GL088365>
- Vos, K., Harley, M. D., Turner, I. L., & Splinter, K. D. (2023). Pacific shoreline erosion and accretion patterns controlled by El Niño/Southern Oscillation. *Nature Geoscience*, 16(2), 140–146. <https://doi.org/10.1038/s41561-022-01117-8>
- Vos, K., Splinter, K. D., Harley, M. D., Simmons, J. A., & Turner, I. L. (2019). CoastSat: A google Earth engine-enabled python toolkit to extract shorelines from publicly available satellite imagery. *Environmental Modelling & Software*, 122, 104528. <https://doi.org/10.1016/j.envsoft.2019.104528>
- Vos, K., Splinter, K. D., Palomar-Vázquez, J., Pardo-Pascual, J. E., Almonacid-Caballer, J., Cabezas-Rabadán, C., et al. (2023). Benchmarking satellite-derived shoreline mapping algorithms. *Communications Earth & Environment*, 4(1), 345. <https://doi.org/10.1038/s43247-023-01001-2>
- Vousdoukas, M. I., Ranasinghe, R., Mentaschi, L., Plomaritis, T. A., Athanasiou, P., Luijendijk, A., & Feyen, L. (2020). Sandy coastlines under threat of erosion. *Nature Climate Change*, 10(3), 260–263. <https://doi.org/10.1038/s41558-020-0697-0>
- Walkden, M., & Dickson, M. (2008). Equilibrium erosion of soft rock shores with a shallow or absent beach under increased sea level rise. *Marine Geology*, 251(1–2), 75–84. <https://doi.org/10.1016/j.margeo.2008.02.003>
- Warrick, J. A., Buscombe, D., Vos, K., Kenyon, H., Ritchie, A. C., Harley, M. D., et al. (2025). Shoreline seasonality of California's beaches. *Journal of Geophysical Research: Earth Surface*, 130(2), e2024JF007836. <https://doi.org/10.1029/2024JF007836>
- Weber, S. B., Weber, N., Ellick, J., Avery, A., Frauenstein, R., Godley, B. J., et al. (2014). Recovery of the South Atlantic's largest green turtle nesting population. *Biodiversity & Conservation*, 23(12), 3005–3018. <https://doi.org/10.1007/s10531-014-0759-6>
- Wildermann, N. E., Barrios-Garrido, H., Jabby, K., Hardenstine, R. S., Shimada, T., Williams, I. D., & Duarte, C. M. (2024). An emerging hazard to nesting sea turtles in the face of sea-level rise. *Global Ecology and Conservation*, 56, e03334. <https://doi.org/10.1016/j.gecco.2024.e03334>
- Willson, A., Witherington, B., Baldwin, R., Tiwari, M., Al Sariri, T., Al Kiyumi, A., et al. (2020). Evaluating the long-term trend and management of a globally important loggerhead population nesting on Masirah Island, Sultanate of Oman. *Frontiers in Marine Science*, 7, 548395. <https://doi.org/10.3389/fmars.2020.00666>
- Wolinsky, M. A., & Murray, A. B. (2009). A unifying framework for shoreline migration: 2. Application to wave-dominated coasts. *Journal of Geophysical Research*, 114(F1). <https://doi.org/10.1029/2007JF000856doi:10.1029/2007JF000856>
- Wright, L., & Short, A. (1984). Morphodynamic variability of surf zones and beaches: A synthesis. *Marine Geology*, 56(1–4), 93–118. [https://doi.org/10.1016/0025-3227\(84\)90008-2](https://doi.org/10.1016/0025-3227(84)90008-2)
- Xu, H. (2006). Modification of normalised difference water index (NDWI) to enhance open water features in remotely sensed imagery. *International Journal of Remote Sensing*, 27(14), 3025–3033. <https://doi.org/10.1080/01431160600589179>
- Yates, M. L., Guza, R. T., & O'Reilly, W. C. (2009). Equilibrium shoreline response: Observations and modeling. *Journal of Geophysical Research*, 114(C9), 9014. <https://doi.org/10.1029/2009JC005359doi:10.1029/2009JC005359>
- Zarifsanayei, A. R., Antolínez, J. A. A., Cartwright, N., Etemad-Shahidi, A., Strauss, D., Lemos, G., et al. (2023). Uncertainties in wave-driven longshore sediment transport projections presented by a dynamic CMIP6-based ensemble. *Frontiers in Marine Science*, 10, 1188136. <https://doi.org/10.3389/fmars.2023.1188136>